J. Mech. Phys. Solids 150 (2021) 104350

Contents lists available at ScienceDirect

Journal of the Mechanics and Physics of Solids

journal homepage: www.elsevier.com/locate/jmps

Image-based multiscale modeling with spatially varying microstructures from experiments: Demonstration with additively manufactured metal in fatigue and fracture

Orion L. Kafka[1], Kevontrez K. Jones, Cheng Yu, Puikei Cheng, Wing Kam Liu *

Department of Mechanical Engineering, Northwestern University, Evanston, IL 60208, United States

ARTICLE INFO

Keywords:
Directed energy deposition
Fatigue
Fracture
Multiscale and reduced order modeling
Process-structure-properties-performance
Uncertainty quantification

ABSTRACT

This manuscript presents a novel modeling framework to predict mechanical performance in material with spatially varying microstructure. The framework combines an efficient process model for AM, a database of experimental 3D images of defects in AM metal, and a microstructure-based multiscale modeling method that leverages recent advances in reduced order modeling. Thus the examples presented will explore heterogeneous and processing dependent dispersion of voids in additively manufactured (AM) metals. The method presented here allows for parametric studies with repeated instantiations of different possible configurations of microstructures (images of defects) throughout the simulated part. Two demonstrations of the method are provided using a database of synchrotron x-ray computed tomography images of porosity collected at the Advanced Photon Source for Inconel 718 built with Laser Engineered Net Shaping®: one case is high cycle fatigue crack incubation and the other is fracture initiation. In both, we show that the model can capture the effects on performance of variability within and between builds. Although not all variability is captured or quantified, the method shows promise for application in AM metals because of its unique ability to mechanistically connect part-scale performance with individual microstructures and the distribution of these microstructures throughout the part.

1. Introduction and motivation

Currently, one major challenge and potential opportunity with additively manufactured (AM) metals is that there exists a large amount of mechanical performance variability within and between builds, for example, in fatigue life and fracture strength (Shamsaei et al., 2015). This results, at least in part, from the highly localized processing strategy. Reports have detailed differences in defect structures, crystalline structures, and composition as a function of location, scan strategy, feed material (e.g. powder size, atomization method), and processing parameters (Mukherjee and DebRoy, 2018; Sanaei et al., 2019; Seifi et al., 2017b; Antonysamy et al., 2013; Lass et al., 2017; Yuan et al., 2018; Zhao et al., 2008; Hohnbaum, 2019). Presently, both truly random and poorly understood yet systematic expression of variability within AM materials is a major cause for concern and lack of confidence with final products (Gorelik, 2017; Seifi et al., 2017a). Conversely, if this variability could be controlled and exploited, new engineered systems could be achieved for example through microscale-aware topology optimization, as surmised in Li et al. (2019a). Previous

* Corresponding author.
E-mail address: w-liu@northwestern.edu (W.K. Liu).
[1] Current address: Applied Chemicals and Materials Division, Materials Measurement Laboratory, National Institute of Standards and Technology, Boulder, CO, USA 80305.

https://doi.org/10.1016/j.jmps.2021.104350
Received 29 July 2020; Received in revised form 20 December 2020; Accepted 31 January 2021
Available online 6 February 2021
0022-5096/

works have accounted for microstructures and/or defects that may vary in space (Horstemeyer, 2010; Li et al., 2019b), or those that arise from additive manufacturing (Yan et al., 2018a; Herroitt et al., 2019). Direct image-based modeling has also been conducted on AM materials, for instance on electron backscatter diffraction maps of electron beam melting metal (Kumara et al., 2018). Gordon et al. (2019) might be thought of as similar, although it only considers monotonic tensile properties for relatively simple build geometries. Prithivirajan and Sangid take another route, and intentionally constructed microstructures with defects similar to those in select laser melting to systematically study the impacts on various performance indicators (Prithivirajan and Sangid, 2018). Other authors have approached the problem of spread in performance using empirical or analytical damage-type modeling, for instance with pre-seeded damage fields or porosity, either synthetically created or from images (Johnson et al., 2019; Pei et al., 2020; Poulin et al., 2020). Note that the majority of these studies have used powder-bed fusion (PBF) or selective laser melting (SLM). Those methods have much higher cooling rates and may impart different performance than powder-fed techniques (Carroll et al., 2015), such as directed energy deposition (DED), which is used in our numerical demonstrations. However, none of these have used modeling to elucidate the effects of process-based variability in microstructure and/or defects in a AM-built part and the potential for both random and systematic variations within a single build or part. There have been recent calls to do just this (Shamsaei et al., 2015; Li et al., 2019c).

In the model proposed here, the fast reduced order modeling approach that accounts for crystallography is combined with a database of X-ray computed tomography images of possible instances of porosity/voids in AM material. This is embedded in a multiscale, multiphysics modeling framework with a finite element representation of the macroscopic (part) scale, and the reduced order model as the microscale (Yu et al., 2019). Variability is captured by assigning different microstructure throughout the macroscopic representation. This assignment can be conducted either to achieve spatially-uniform randomness (bulk homogeneous response) or spatially-varying randomness (bulk heterogeneous response). To model additive manufacturing, microstructures are selected based on the outputs of a model of the AM process, which estimates the void volume fraction at each point in the part. In this way, the process informs the final mechanical predictions, and thus might be used in design or used to construct and virtually measure the impact of specific desirable (or undesirable) configurations of microstructures on the macroscale part performance.

This work relies upon our recent developments in reduced order and multiscale modeling, in concert with 3D imaging experiments for additively manufactured metals. These combine a data-driven micromechanics method called self-consistent clustering analysis (SCA) with computational crystal plasticity (CP), termed crystal plasticity self-consistent clustering analysis (CPSCA). This method as applied to crystal plasticity was first introduced by Liu et al. (2018). Shakoor et al. (2018) and Yu et al. (2019) extended this to a finite strain formulation to be fully compatible with deformation-gradient-based CP, and demonstrated a concurrent multiscale model. A microstructurally relevant Fatemi–Socie fatigue indicating parameter (FIP) (Shenoy et al., 2007) was computed with this approach by Kafka et al. (2018).

The primary goal of this paper is to describe a new method that integrates the above-noted features. The resulting framework has several unique features:

- A physical basis for the microstructure geometry and high fidelity than synthetic, imagined, or idealized microstructures, using a database of 3D experimental images as the microstructural representation of the microscale directly in a concurrent multiscale model
- Location- and process/history-dependent properties and performance prediction, demonstrated here using CPSCA
- Scalability to incorporate microstructure in components or systems (based on the macroscale representation)
- Ability to estimate variability, in addition to mean/min/max, in mechanical performance throughout the domain without recourse to statistically generated microstructure or inference. In this work fatigue life or fracture initiation point are the two example measures of mechanical performance.

Other recent modeling efforts have been developed to predict the impact of microstructures and defects on part performance. Fast Fourier Transform (FFT)-based methods have proven popular due to computational efficiency; for example, Liu et al. (2019) show a framework that connects a phase-field based method for grain prediction with a FFT-based crystal plasticity method for performance prediction, while Eghtesad et al. (2018) present what they term a spectral database constitutive model for computational crystal plasticity based around the FFT method. Pei et al. (2020) propose a homogenized damage-based method that accounts for progressive damage to the materials using accumulated plastic strain in combination with a weighed parameter thought to represent damage from voids and inclusions. Whelan and McDowell (2019) and Tallman et al. (2020) both discuss the importance of uncertainty quantification when modeling fatigue in polycrystalline materials. The latter also discusses variability at different length scales, and information propagation between scales, but it does not consider a full component-level simulation (Tallman et al., 2020). However, none of these directly capture the location-based and process-based variability as done by the method proposed herein.

The paper will propose the method (Section 2), and give two computational demonstrations (Section 3). The method description first starts with an overview (Section 2.1), and second describes how the preliminary database of microstructures is generated (Section 2.2). Third, the thermal model of the AM process is described (Section 2.3), followed fourth by a description of the macroscale stress analysis (Section 2.4), and followed fifth by a description of the microstructure selection and reduced order modeling technique used at the microscale (Section 2.5). This is followed by the two examples: first a prediction of the strain-life fatigue behavior of a sample of virtual fatigue specimens built of Inconel 718 (IN718) with several different process parameters (Section 3.1), and second an estimate of the fracture initiation behavior of a compact tension specimen (Section 3.2).

2. Methodology

The overall goal of this methodology is to provide a mechanistic multiphysics multiscale framework with which components consisting of spatially-varying microstructures can be (a) constructed and (b) analyzed for mechanical response or performance (e.g., fatigue or fracture). The primary motivation for such a mechanistic framework is additively manufactured metals with spatially heterogeneous microstructures, both in terms of defects, such as voids, and crystallography. In order to construct a computational methodology, several different simulations and numerical techniques are interconnected to construct a broadly applicable workflow that combines process modeling and stress analysis to estimate mechanical performance on the component scale, as defined by microstructural response to mechanical loading on the component scale. A conceptual schematic of this overall idea and the role of each component is given in Fig. 1.

2.1. Model setup and overview

Conceptually, this multi-physics, multiscale method is implemented as a series of coupled analyses, some of which are themselves concurrent or hierarchical models. It is multi-physics because it connects a model of the AM process that outputs thermal history by solving the heat equation, to a model that predicts mechanical response by solving the equilibrium equations. It is multiscale because to solve for the mechanical response, the problem is described in terms of two different representations: the macro- or part-scale, and the microscale that represents individual microstructures. The modeling process leading from thermal analysis to mechanical performance (e.g., fatigue or fracture) is outlined step-by-step in Box I. Functionally, the thermal analysis takes as input processing conditions and part geometry, and outputs local thermal conditions (e.g., thermal gradient (G), its velocity (R), or the solidification cooling rate (SCR)) represented by a list of x, y, z coordinates and their corresponding thermal variables. A correlation function takes in local thermal information and outputs an array of possible microstructures for each material point in the mechanical mesh of the component; if necessary, thermal results are averaged to the coarser mechanical mesh before the selection is made. On that basis, an instantiation that selects one specific microscale for each macroscale material point is generated. This instantiation is used to conduct a stress analysis with either one-way or two-way coupling to predict local (microscale) and component (macroscale) material response.

In order to accomplish this, before the analysis is conducted, a database is constructed that contains a broad selection of possible microstructures. For example, if the critical, performance limiting microstructure is porosity (as later demonstrated), this could be embodied by images of different pores that might occur in AM material. In the demonstration cases given below, solidification cooling rate is related to void volume fraction, following the relationship proposed in Wolff et al. (2017), because our experimental data consists of images of voids rather than the example for grains given above.

Box I **Overall modeling process with this framework**

The process for a particular component of interest is as follows:

1. Macroscale thermal model of the build process, which provides a local, microstructurally relevant measure that captures the influence of processing parameters (scan speed and laser power are shown as examples).
2. Generation of a possible instance of the overall specimen by picking subset images (microstructures) for every point in the component that match the relationship between processing history and microstructural descriptors developed in the preliminary step.
3. Stress analysis to compute the deformation history of the component and its microstructures
    (a) For one-way coupling: compute macroscale deformation history, then for every microstructure associated to a point in the component, apply the deformation computed in the macroscale stress analysis of the component for that point.
    (b) For two-way coupling: run the concurrent model with the predefined microstructures presenting their respective material points.
4. Computation of the performance of the component based on a performance metric applied to each microstructure. For example, the minimum fatigue life within a microstructure will give the failure location and cycles-to-failure.
5. Repeat steps 3-5 until a reasonable confidence of the results, based on possible microstructural configurations, is obtained.
6. Repeat steps 1-6 and/or 2-6 for different processing conditions and/or loading conditions as needed.

This overall scheme is shown graphically in Fig. 2 with a generic example component, where pores are the critical microstructure and a database has been built from XCT images of pores in AM. The different steps of this method make use of different solution methods, conducted in several different software packages (both internal codes and commercial software). However, the data exchange between each step requires little user input and could be set up to operate automatically if required for parametric studies. The different tools used through this framework have been validated independently, and citations to the articles in which more thorough validation has been carried out for each of these components are provided.

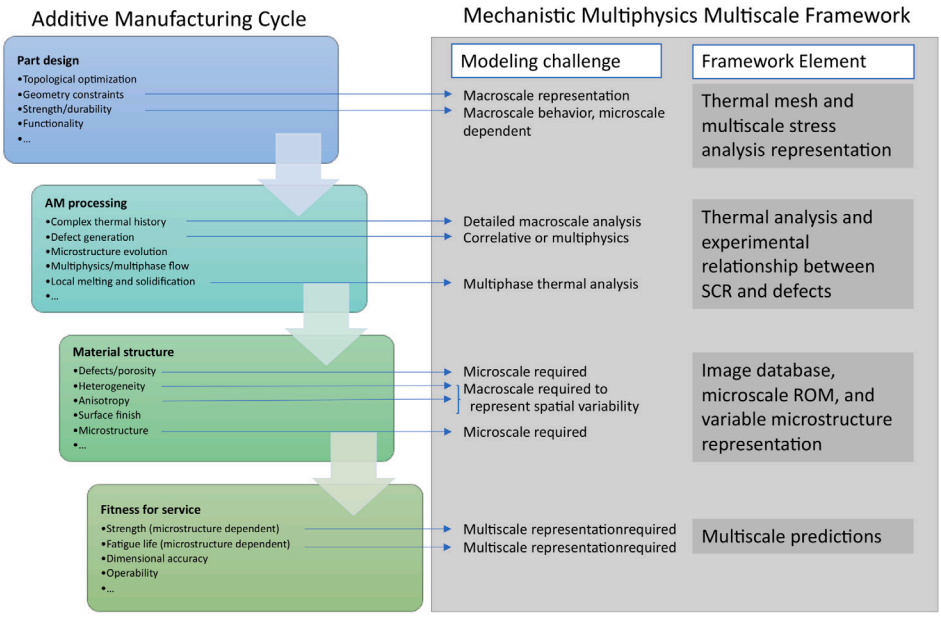

Fig. 1. A conceptual representation of the significant complexities involved in additive manufacturing, from part design to final performance. The right column contextualizes this with the aspects addressed by, and the relationship with, the elements of the current mechanistic multiphysics computational framework.

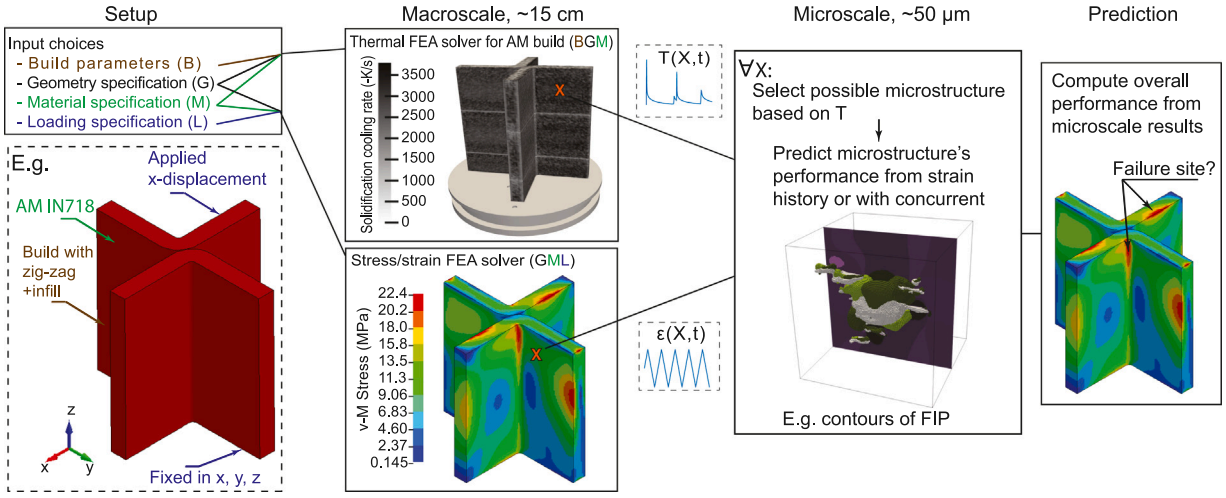

Fig. 2. Overall diagram of the computational scheme. Geometry, build process parameters, material, and loading conditions must be specified. These inputs are used to conduct a thermal analysis and a macroscale stress analysis. For each material point X, the thermal data is used to select an element-wise microstructural sub-model, and the stress–strain solver is used to provide local boundary conditions, representing a possible state at that point. Each microstructure is used to predict the local, microscale evolution of state variables such as plasticity and damage, which are homogenized (e.g. by taking the l_∞ norm of the domain) and used as element-wise estimators of part-level susceptibility to failure.

2.2. Experimental image database generation

In general, the database used in this framework should contain some relevant microstructure, and a record of some property of that microstructure that can be related to a local measurement that depends on processing history, for instance grain sizes/shapes/orientations, porosity sizes/shapes/orientations, inclusion content, and/or dislocation densities. One critical requirement of the current implementation is that both measures must be local, i.e., e.g., smaller than a single molten pool. This requirement comes from the assumption of scale separation built into the multiscale method used for performance analysis — the microstructural representation of each material point needs to be much smaller than the size of the finite element in which that material point resides. The selection of measurements of (local) processing history and microstructure properties requires a link between the two.

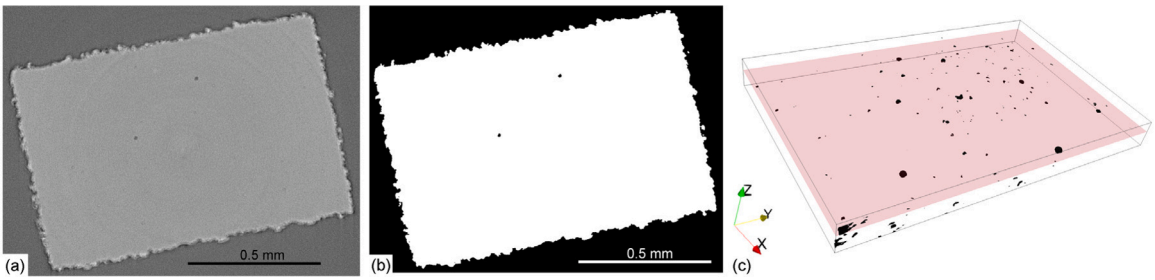

Fig. 3. XCT image processing steps (a) Slice from reconstruction (b) after filtering and thresholding (c) the 3D region (150 slices) around the slice in (a) and (b), with that slice highlighted, after all processing steps.

A relationship between the predicted thermal history and microstructure descriptors is used to identify possible defects at each location in the build. In principle, a number of different relationships could be used based on scientific knowledge of the system. The most basic, and probably incorrect, would be a uniformly random distribution of microstructure throughout the part. However, results from literature and our prior experience, e.g. Wolff et al. (2017) and/or Parimi et al. (2014) indicate that there are trends in microstructure that depend on thermal history and conditions that can be exploited. In this paper, we focus on porosity as this is likely the critical microstructure for fatigue and fracture, and use void volume fraction V_f as its measure. The overall V_f is computed from the simple sum of the pore sizes throughout the image for each location, similar to Wolff et al. (2017) but using 3D measurements with XCT. Because many images might have the same or similar V_f based on this measure, the database contains many repeated possibly microstructures for each V_f. Selecting one possible microstructure for each point in the build thus gives one "instance" of that component.

To collect images with varying void volume fraction X-ray tomography imaging experiments from Advanced Photon Source (APS) Beamline 2-BM, Argonne National Laboratory were used. Two as-built (with a solutionizing stress relief heat treatment) "thin wall" geometries one track wide were built with Laser Engineered Net Shaping® (LENS, a trade name which will be used interchangeably here with DED). From these thin walls, specimens were extracted and scanned from 22 locations on each wall (total 44 specimens). Each image contained between $1\,\text{mm}^3$ and $2\,\text{mm}^3$ of material, with a voxel edge length $0.65\,\mu\text{m}$. Three-dimensional images were reconstructed using a customized version of Tomopy, based on version 1.0.1 (Gürsoy et al., 2014). In the 3D images, contrast from X-ray absorptivity was used to distinguish between pores and material. After reconstruction, a stack of 8-bit grayscale tiff images were loaded into a MATLAB parallel image processing script. This script applied a series of *localcontrast*, median, and Gaussian filters before invoking the *graythresh* and *imbinarize* utilities to convert the grayscale images to binary images. The final binary images still contained occasional scanning artifacts, mostly rings. These were identified by another script before being manually verified as artifacts and removed from the binary images. Fig. 3 shows (a) an example grayscale image from reconstruction, (b) a binary version of that slice, (c) a 3D rendering of the final volume with voids in black and the slice shown in (a) and (b) highlighted. For more details regarding the imaging experiments, see Kafka (2019).

The image database is comprised of many small images, each of size $97.5\,\mu\text{m}$ by $97.5\,\mu\text{m}$ by $97.5\,\mu\text{m}$ (150 voxels in each dimension), extracted from the 44 full-size tomography images. These were referred to as "sub-images" because they define a bounding box around subregions of the full-size image. These sub-images were chosen at strategic locations such that the pore volume fractions within the bounding box, V_f, lie within the range of V_f determined in Appendix B. To build the database, a search process through the larger images was conducted for the appropriate sub-image locations. First, candidate bounding box locations were uniformly generated within the full-size image. After checking that the bounding box did not overlap with bounding boxes already in the database and "filling in" pores that intersect with the bounding box boundary. These boundary pores were removed to enable the use of periodic boundary conditions in simulations. Then, if the bounding box was calculated to contain an appropriate pore volume fraction V_f, the data within the bounding box is entered into the sub-image database.

The final database contains sub-images with $V_f \approx 0.0001$ to $V_f \approx 0.03$, include the geometry, clustering, and interaction tensor for each as shown in the diagram in Fig. 4. A total of 388 different example sub-images of pores were extracted. The database indexes the sub-images by their V_f so that the appropriate sub-image can be retrieved from the database given a desired V_f. Of these, 320 were used in the computational demonstrations shown in Section 3. A subset of the total number of extracted sub-images were used in order to more closely match the histogram of expected V_f and the histogram of V_f in the available images. This involved removing, at random, most of the very high and very low V_f sub-images.

Once the microstructure database entries were collected and curated, the three training steps outlined in Section 2.5.2 were conducted on each entry. Thus, the final database used for the multiscale mechanical response prediction contains proto-data used to generate response predictions for arbitrary loading, which depends upon microstructural information. Thus, all the mechanical response predictions shown in the following sections and in the numerical demonstrations are computed directly with 3D XCT sub-images of pores in IN718 build with LENS. For our purposes of demonstrating this framework, this is sufficient. However, one could imagine populating the same kind of database more completely with not only pores but also different crystallographic structures, different phases, etc. For example, microstructures synthetically built with DREAM3D based on statistics of defects or microstrcutures measured experimentally, or directly generated from process simulations as in Yan et al. (2018a) might also be used. For simplicity and demonstrative purposes the examples shown here will only consider pores — the most critical defect for surface finished material.

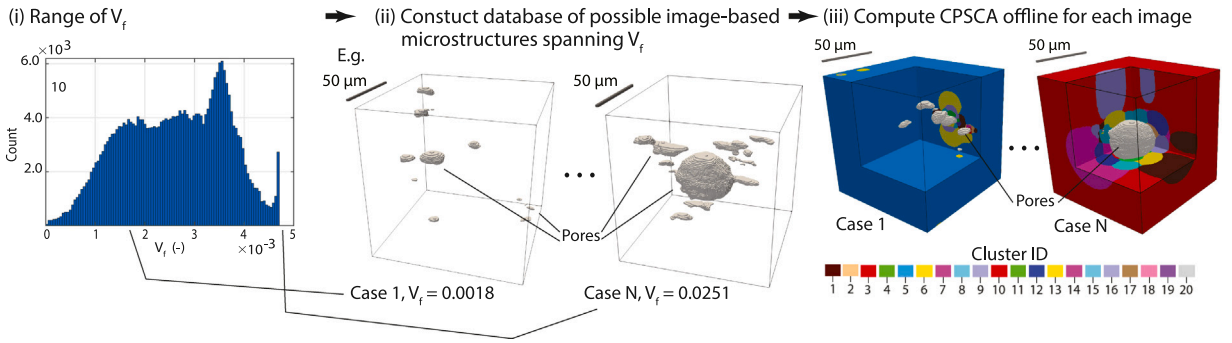

Fig. 4. Microstructure database setup: in this example, a set of XCT image subsets are extracted such that the volume fraction (V_f) of the extracted sub-images span the range of expected V_f within the part to be modeled. The "offline" part of the reduced order model at the microscale (explained in more detail later) is computed for each of these subset images, and the resulting collection of subimages constitutes a database from which microstructure images are selected.

2.3. Thermal modeling for the AM build process

A thermal analysis is used to model building the component of interest using the directed energy deposition (DED) method. This analysis is done using a transient thermal finite element solver called GAMMA (Smith et al., 2016). The specific equations solved by the code are provided in Appendix A.

The physical build parameters, including laser speed and power and the scan strategy, must be selected. The material must also be specified, along with other modeling parameters such as the mesh and boundary conditions. With this information given, the model can predict the time–temperature-history of each point within the part. This is achieved by specifying elements in the mesh to activate or de-activate based on the time-history of the scan strategy: elements that the tool has traversed are considered activated, and are included as fully dense material, while elements that the tool has yet to traverse are not included in the thermal solution. Moving boundary conditions are employed that account for active and inactive elements, appropriately applying the heat transfer conditions as required throughout the domain.

The solidification cooling rate (SCR) is calculated based upon the temperature history of the thermal model at each node. This is approximated according to Eq. (1) at each material point, represented by subscript i, as the ratio of the difference between solidus temperature and liquidus temperature to the difference between the time at which the liquidus and the solidus temperature is reached; i.e. the average rate of temperature change in the solidification region.

$$SCR\left(\mathbf{X}^M\right) \approx \frac{T^{liquid}\left(\mathbf{X}^M\right) - T^{solid}\left(\mathbf{X}^M\right)}{t^{liquid}\left(\mathbf{X}^M\right) - t^{solid}\left(\mathbf{X}^M\right)} \quad \forall \mathbf{X}^M \in \Omega^M \tag{1}$$

where $SCR(\mathbf{X}^M)$ is the solidification cooling rate as a function of the macroscale spatial coordinates $\mathbf{X}^M$ within the macroscale domain Ω^M, $T^{solid}\left(\mathbf{X}^M\right)$ is the solidus temperature, $T^{liquid}\left(\mathbf{X}^M\right)$ is the liquidus temperature, $t^{liquid}\left(\mathbf{X}^M\right)$ is the time at which the liquidus temperature is reached, and $t^{solid}\left(\mathbf{X}^M\right)$ is the time at which the solidus temperature is reached. In order to capture this solidification behavior, Eq. (A.1) is solved explicitly with an approximate time step of 9.0×10^{-4} s. If too large of a timestep is chosen, one may skip over the solidification behavior at some material points. Additionally, in the case of re-melting, only the final cooling stage is considered. The SCR during final solidification (if melting and re-solidification occurs) is saved as an output parameter.

The thin wall geometries from which specimens were extracted for XCT were also used to validate the thermal model. To accomplish this, a simulation mimicking the experiments outlined by Bennett et al. (2018) was conducted. Bennett et al. (2018) report the solidification time for a few points in the build, which can be converted into SCR values using Eq. (1). However, due to the limited amount of experimental data provided, only the range of SCR values between the reported points with the largest and smallest solidification times were compared. As seen in Fig. 5, the experiment and the simulation are on the same order of magnitude but the simulation gives an under-prediction. This is not surprising, since the we are using a conduction-based thermal model. If, for instance, cooling affects within the melt pool were considered, the SCR values would increase (i.e. the solidification time would decrease). Considering this expected behavior and the potential uncertainties in the measurements (as noted in Bennett et al., 2018, these measurements are mostly useful for relative comparisons due to large possible experimental error from various factors), this level of agreement is acceptable to us.

2.4. Macroscale stress analysis

At the macroscale, a stress analysis representing expected service-life conditions of the component or specimen is conducted. This is conducted using the finite element method, solving the equilibrium equation with boundary conditions appropriate for the expected service life. For loading conditions where a small strain approximation is valid (e.g. below the elastic limit of the material for IN718), an elastic model or well-known elasto-plastic model, such as Johnson–Cook, with one-way hierarchical coupling is sufficient with either implicit or explicit time stepping at the macroscale. The time history of the deformation gradient at each

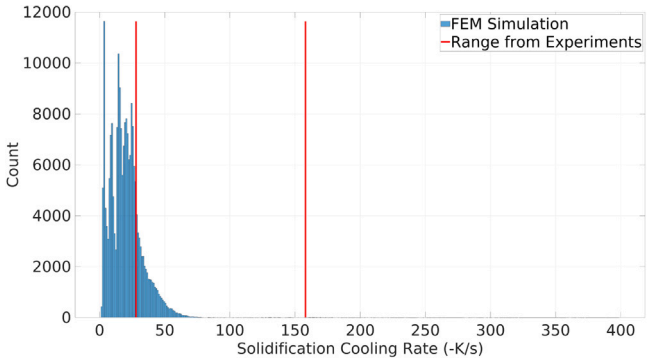

Fig. 5. Comparison of predicted SCR values from the thermal model against an experiment (Bennett et al., 2018). Here the range from the experiments is defined by the smallest and largest reported solidification times.

material point in the FE solution is extracted, to be passed to the microscale model. In cases where significant plastic strain or finite deformations are to be considered, a concurrent coupling is used instead, with implicit timestepping for the finite element solution. In the concurrent scheme, the effective response of the microscale is directly used to compute the stress–strain response for the macroscale material model, replacing the constitutive model. A concurrent implementation for materials that are well-described by single RVE has been demonstrated by Yu et al. (2019), and is adapted for use here. These two operating modes are exemplified in the numerical examples for fatigue and fracture, respectively.

2.5. Microscale performance prediction

Two steps are used to make microstructure-based predictions. First, a microscale is selected for each material point in the macroscale based on predetermined criteria (Section 2.5.1). Second, the mechanical response of that microstructure is analyzed given the macroscale deformations at that point (Section 2.5.2). A schematic of these processes is shown in Fig. 6, where the local temperature history and strain history are taken as inputs to a micromechanics model, which then computes local and homogenized stress/strain responses. In this case several computational homogenizations of the microscale have been conducted. The two most important are the l_∞ norm of the FIP and the volume average of the stress, with the former being used for fatigue potency prediction and the later being used to inform the stress response for the concurrent multiscale, as described in detail in Yu et al. (2019). The performance measurement depends on the property of interest, with two demonstrations given: one for fatigue and one for fracture. The figure illustrates a fatigue example.

2.5.1. Microstructure selection

To select the microstructure that represents each macroscale material point the relationship described in Appendix B is used to link solidification cooling rate from thermal model and void volume fraction, following the findings of Wolff et al. (2017). With this approximation of V_f, we then assume that any microstructure in the database within 20% of the predicted V_f has equal probability of occurring. In this way, the part is described by essentially a Monte Carlo process, where the bounds of the random variable (in this case the exact configuration of pores bounded by V_f) are controlled by the process model. This is shown schematically in the top right of Fig. 6. in Appendix C gives the detailed algorithm for selecting, for each material point, the entry in the database to use following the explanation above. Note that because number of images in the current database is smaller than the number of macroscale material points for the examples shown in Section 3, each image might be selected multiple times in each specimen and the same database is used for all specimens. In practice, in the demonstrations shown having between about 5 and 10 microstructures to pick from at random in each point is common, and each microstructure in the database might be selected between zero and perhaps several hundred times. While a larger database would enable less repetition, and thus allow greater variability and higher fidelity, this is sufficient to demonstrate our method and generally pore distributions on the microscale might have similar features (e.g. a linear group of pores caused by insufficient melting, or a large pore caused by melt pool fluctuations).

2.5.2. Microscale mechanical response: reduced order model with crystal plasticity

Once a microstructure is chosen, the reduced order mechanical modeling approach at the microscale is applied. In essence, the microscale fatigue prediction model used here is the same crystal plasticity material representation as in Kafka et al. (2018), but calibrated to IN718. The fracture prediction model is more closely tied to the multiscale concurrent system shown in Yu et al. (2019), which shares the reduced order modeling technology derived from Liu et al. (2016).

Briefly, the method, CPSCA, solves the mechanical equilibrium equations by breaking the problem into two stages. The first “training” stage consists of three steps: data collection (identifying the microstructure), data compression (or clustering), and computation of the interaction tensor. The resulting interaction tensor is stored for future use. The second “prediction” stage makes use of the interaction tensor and solves the discretized form of integral equation given in Appendix D subject to an applied strain state and material law. The overall process is shown for an example entry in the database in Fig. 7.

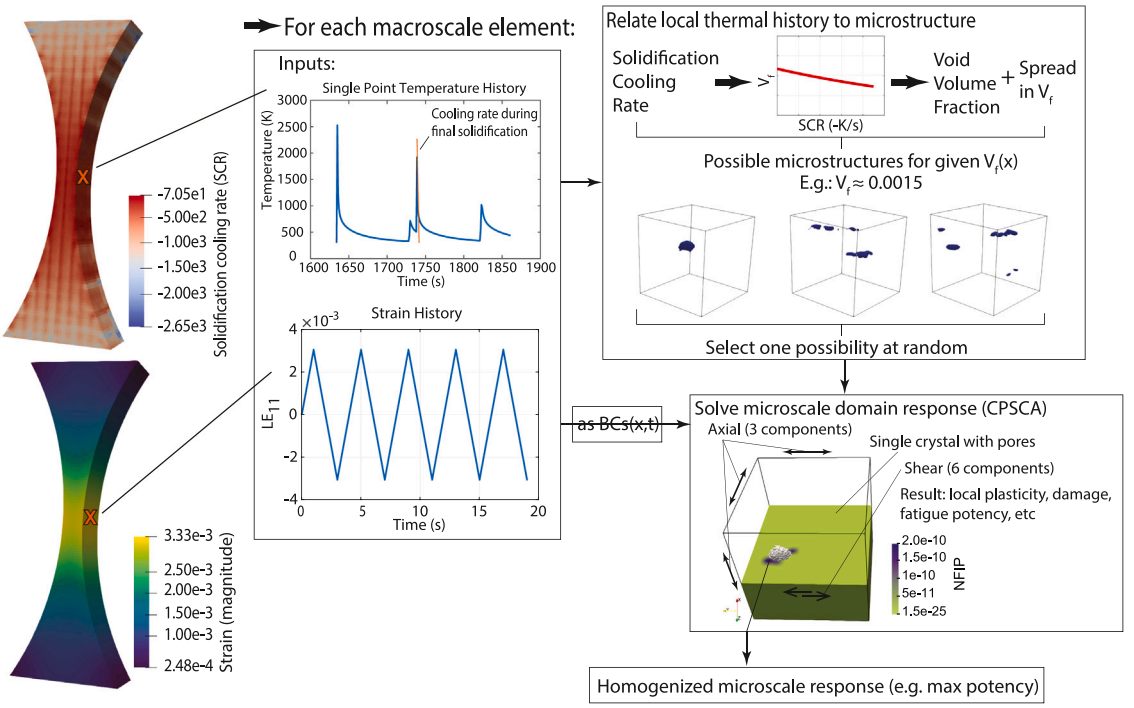

Fig. 6. Overview of the solution process for each macroscale material point (in this case, within the dogbone specimen used in the numerical example in Section 3), the thermal history and strain history are passed to a microscale solver; a microstructure is selected using the relationship described in Appendix B based on the thermal history, and deformation boundary conditions are applied according to the deformation history. A crystal-plasticity-based microscale solution is computed, and a homogenized response (e.g. the l_∞-norm of the fatigue indicating parameter for fatigue, or the number of failed clusters for fracture) is returned to the macroscale.

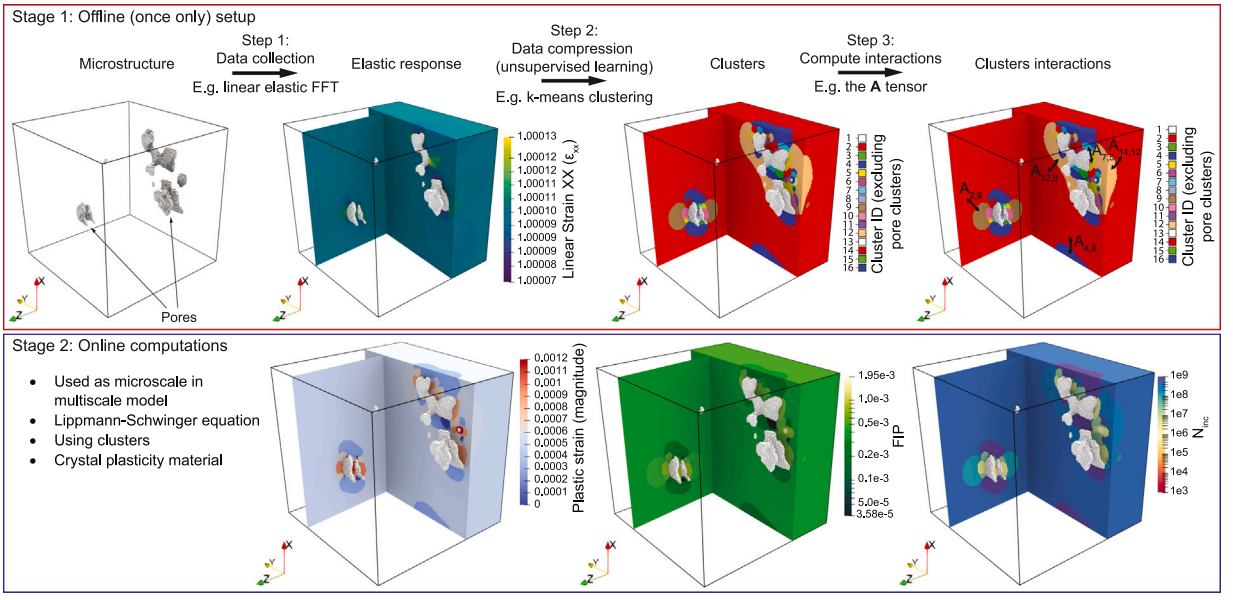

Fig. 7. The CPSCA process: offline setup and online computations for an example microstructure within the database. The offline steps are run once and the resulting cluster distribution and interaction tensor are included in database. The online computations are used throughout the simulations to predict stress, plastic strain, etc.

This first stage is conducted for each of the subset volumes created, adding the clustering and interaction tensor data to the database of image subsets. This defines the completed "microstructure database". After a part is instantiated (microstructures

selected from the database for each macroscale point), only the second stage has to be used to compute the mechanical response. The second stage is very fast to run without the first stage, and can be run any number of times with new, independent stress–strain histories and boundary conditions without re-running the first state. Thus, different behavior at different points in the macroscale can be predicted rapidly using the pre-built database of the first stage data. The CP model used here for the second stage takes as input increments of applied deformation gradient, as defined by the macroscale as boundary conditions at the microscale, and supplies local stresses and deformation variables (such as the plastic part of the deformation). This is effectively the same paradigm as is shown in Kafka et al. (2018) and Liu et al. (2018), applied here as at the microscale of a multiscale modeling framework. The applied deformation gradient, $\boldsymbol{F}$, is multiplicatively decomposed into an elastic and a plastic part, $\mathbf{F} = \mathbf{F}^e\mathbf{F}^p$; the plastic part of the deformation gradient, $\boldsymbol{F}^p$, is computed from the plastic velocity gradient (represented as an intermediate configuration, as described in, e.g., Belytschko et al., 2013) $\tilde{\mathbf{L}}^p$, which itself is determined by summing the plastic shear velocity across slip systems in an intermediate configuration. This plastic shear velocity (in the intermediate configuration) is defined by crystallographic and materials factors, as:

$$\tilde{\mathbf{L}}^p = \sum_{\alpha=1}^{N_{slip}} \dot{\gamma}^{(\alpha)} \left(\tilde{\mathbf{s}}^{(\alpha)} \otimes \tilde{\mathbf{n}}^{(\alpha)}\right) \tag{2}$$

where N_{slip} is the number of slip systems, $\dot{\gamma}^{(\alpha)}$ is the shear rate of slip system α, $\mathbf{s}^{(\alpha)}$ is the slip direction of slip system α, and $\mathbf{n}^{(\alpha)}$ is the slip plane normal of slip system α. The symbol $\otimes$ describes the dyadic product. A phenomenological power law is used to define the shear rate for each slip system:

$$\dot{\gamma}^{(\alpha)} = \dot{\gamma}_0 \left| \frac{\tau^{(\alpha)} - a^{(\alpha)}}{\tau_0^{(\alpha)}} \right|^{(b-1)} \left(\frac{\tau^{(\alpha)} - a^{(\alpha)}}{\tau_0^{(\alpha)}} \right), \tag{3}$$

where $\tau^{(\alpha)}$ is the resolved shear stress defined by $\tau^{(\alpha)} = \boldsymbol{\sigma} : (\mathbf{s}^{(\alpha)} \otimes \mathbf{n}^{(\alpha)})$ where $\boldsymbol{\sigma}$ is the Cauchy stress, $a^{(\alpha)}$ is a backstress that describes kinematic hardening, $\dot{\gamma}_0$ is a reference shear rate, $\tau_0^{(\alpha)}$ is a reference shear stress that accounts for isotropic hardening, and b is the material strain rate sensitivity. The reference shear stress $\tau_0^{(\alpha)}$ evolves based on direct hardening and dynamic recovery terms. The reduced order model predictions for void deformation in IN718 have been experimentally validated against in-situ XCT tensile test observations shown in Yu (2019) and Kafka (2019).

In the case of one-way coupling, the full deformation gradient history from the macroscale analysis is passed to the microscale. Failure is assessed at the microscale, and a single statistic, e.g. minimum number of cycles to failure for fatigue, is used to assess the variation across the macroscale. The two-way concurrent multiscale coupling is required for convergence of the CP method in the fracture example, to account for the larger strains. In this case, the entire online portion of the CPSCA is implemented as a custom user material subroutine that passes the homogenized microscale stress back to the macroscale for each increment of the analysis, using a modification of the implementation reported in Yu et al. (2019).

2.5.3. Example performance measure: fatigue life

Fatigue life is measured using Shenoy and McDowell's modification to the Fatemi–Socie fatigue indicating parameter (FIP) (Shenoy et al., 2007). The formulation is the same, implemented within CPSCA using the same routines as described in Kafka et al. (2018). In this work the FIP equation is

$$FIP = \frac{\Delta\gamma^p_{max}}{2}\left(1 + \kappa\frac{\sigma_n^{max}}{\sigma_y}\right), \tag{4}$$

where FIP is the fatigue indicator parameter computed from the maximum of the cycle-to-cycle change of the plastic shear strain, $\Delta\gamma^p_{max}$, the stress normal to $\Delta\gamma^p_{max}$, σ_n^{max}, the normal stress factor κ (assumed to be 0.55 here), and the material parameter yield stress, σ_y. A volume averaging region to account for non-locality and set a length scale is set with edge length l_{avg} equal to 10% of the edge length of the equivalent cube edge length of the total void volume (i.e. $l_{avg} = 0.1\sum(\text{voidVolume})^{1/3}$). The volume averaged FIP value saturates after a few cycles of loading. For a reference defect-free condition the relationship between maximum FIP and fatigue is calibrated to literature data for fatigue of IN718 with

$$NFIP_{max} = \bar{\gamma}_f \left(2N_{inc}\right)^c \tag{5}$$

where $NFIP_{max}$ is the maximum non-local FIP, N_{inc} is the number of fatigue incubation cycles, and $\bar{\gamma}_f$ and c are the fitting parameters. After the law is fit in a separate set of simulations, the fitting constants are used in the concurrent simulations. The FIP, and subsequent N_{inc}, are computed from the stress and plastic shear strain computed by the crystal plasticity law defined above.

2.5.4. Example performance measure: fracture potency

The fracture potency is estimated by computing the local microscale Lode parameter and stress triaxiality and comparing that to a failure criterion applicable to microscale deformations. These measures account for, e.g., pore–pore interaction causing local stress enhancement. The initiation of fracture during loading is predicted in this way using the multiscale model. Note that this enforces fracture initiation to occur within one or more microscales, and due to the scale-separation assumption there is no potential for direct interaction between microscales.

Table 1
Thermo-physical properties of IN718 (Mills, 2002).

Property	Notation (Units)	Value
Density	$\rho\ \left(\frac{\text{kg}}{\text{m}^3}\right)$	8100
Solidus temperature	T_s (K)	1533
Liquidus temperature	T_l (K)	1609
Specific heat capacity	$c_p\ \left(\frac{\text{J}}{\text{kgK}}\right)$	$360.24 + 0.026T - 4 \times 10^{-6}T^2$
Thermal conductivity	$k\ \left(\frac{\text{W}}{\text{mK}}\right)$	$0.56 + 2.9 \times 10^{-2}T - 7 \times 10^{-6}T^2$
Latent heat of fusion	$L\ \left(\frac{\text{kJ}}{\text{kgK}}\right)$	272

Table 2
Sets of process parameters for thermal analysis of IN718, similar to the experimental values reported in Bennett et al. (2018).

Parameter set	1	2	3
Laser power, P (W)	1800	1800	1800
Scan speed (mm/s)	15	10	15
Beam radius, R_b (mm)	1.5	1.5	1.5
Layer thickness (mm)	0.75	0.75	0.75
Scan strategy	zig-zag	zig-zag	unidirectional

3. Model prediction results: two computational demonstrations

Two example cases, one for fatigue and one for fracture, are given below. Each follow the relevant ASTM standard geometry, and in both cases a mesh refinement study was conducted to ensure converged results at the macro-scale, where convergence was estimated both visually in terms of overall stress contours and by measuring the difference in maximum stress and ensuring this was sufficiently small between the mesh selected and the finest mesh, taken as the reference solution, when using a simple material model (i.e. Johnson–Cook) at the macroscale. Because of computational expense, a similar mesh refinement was not conducted using the concurrent multiscale; we assume that a converged mesh using the simple material model will be sufficient also for the concurrent material model. The maximum image resolution is used at the microscale, and convergence of the reduced order model has been shown in previous work (Yu et al., 2019).

3.1. Fatigue life prediction

A fatigue specimen conforming to the ASTM E466 standard geometry (ASTM, 2015) is numerically built and tested. The specimen geometry was meshed with two different hexahedral meshes, for one thermal analysis (the "thermal mesh") and one stress analysis (the "stress mesh"), as shown in Fig. 8. The two meshes are largely the same, except the mesh used for stress analysis is coarsened in the thickness (z-) direction. This is the build direction, and thus requires at least one element per build layer in the thermal model, but during the stress analysis the stress and strain are nominally constant through this direction. This may, however, smooth out some of the variability between process parameters, as SCR was averaged during mesh coarsening. Following the schematic shown in Fig. 2, this mesh was loaded into both the thermal solver and, slightly modified, in the stress solver.

An in-house thermal FEA solver was used for the thermal model. The thermal properties for IN718 are summarized in Table 1. For the thermal analysis, two scan strategies were simulated, one with a zig-zag pattern and 90-degree layer-by-layer offset (Fig. 9(a)) and another with a unidirectional pattern (Fig. 9(b)). Similar scan strategies have been reported in the literature, and our understanding is such patterns are commonly used in experimental settings (Tabernero et al., 2011; Liu et al., 2011). Two different sets of process parameters, similar to those used by our experimental collaborators (Bennett et al., 2018) and elsewhere in the literature Jinoop et al. (2019), are specified in Table 2. The part was meshed and simulated with the gage section aligned normal to the build direction. A relatively fine mesh with 539216 hexahedral elements (Fig. 8(a), substrate not shown) was used; Fig. 8(b) shows a detail of the mesh in the narrowest part of the gage section. Simulation times for the thermal analysis were 393.6 CPU hours for parameter set 1, 638.4 CPU hours for parameter set 2 (with slower scan speed), and 408.0 CPU hours for parameter set 3, running on 24 Intel Xeon Haswell E5-2670v3 CPUs at 2.3 GHz clock speed.

For the macroscale stress analysis of the fatigue coupon, reduced integration hexahedral elements with hourglass control were used to compute stress and deformation using implicit timestepping. The lower grip was fixed and the upper grip was displaced at constant displacement rate over four fully reversed load cycles. Several different strain amplitudes with repeated instantiations at each strain amplitude were run at constant ambient temperature. For the macroscale analysis, the Johnson–Cook plasticity parameters identified by Farahani et al. (2017) were used as shown in Table 3, although under the fatigue loading specified the macroscale response was entirely elastic, so the Johnson–Cook plasticity routines were never invoked.

The CPSCA method outlined in Section 2.5.2 was used at the microscale. The parameters for crystal plasticity were calibrated by minimizing the difference between many runs of a cubic domain consisting of 64 cubic grains and a set of baseline tensile and cyclic loading data for AM IN718, with starting conditions taken from Cruzado et al. (2017) (for m and $\dot{\gamma}_0$) and Ghorbanpour et al.

Table 3
Macroscale material properties used for one-way multiscale modeling (fatigue), from Farahani et al. (2017), for the commonly-used Johnson–Cook material law. The response is fully elastic so these are only included for completeness, and were never used in the computation of this example.

Parameter	E (GPa)	ν	A (MPa)	B (MPa)	n	m	C
Value	177.0	0.273	1108	699.0	0.5189	1.2861	0.0085

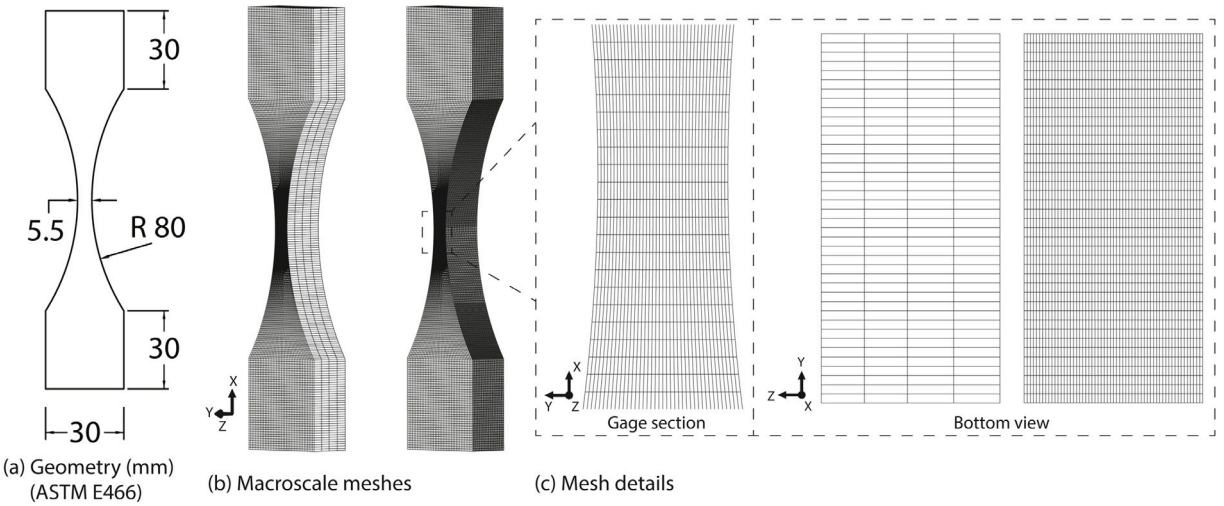

Fig. 8. ASTM E466 fatigue specimen with (a) dimension specifications (b) the two meshes and (c) details of the specimen meshes, including the difference between stress (left) and thermal (right) meshes.

Table 4
Primary crystal plasticity model parameters.

Parameter	Value
C_{11} (MPa)	257,000
C_{12} (MPa)	127,000
C_{23} (MPa)	94,000
$\dot{\gamma}_0$ (s^{-1})	0.0024
m	60
τ_0 (MPa)	360

Table 5
Fatigue indicator parameter values.

Parameter	Value
σ_y (MPa)	750.0
κ	0.55
γ_f	0.0059
c	−0.1317

(2017) (for elastic moduli). The resulting model parameters are given in Table 4. The parameters that relate FIP to fatigue life were fitted to experimental high cycle fatigue data of IN718 collected from literature Kirka et al. (2017), Yan et al. (2003), Texier et al. (2016), Zhang et al. (2013), Amanov et al. (2015), Chen et al. (2005), Belan (2015), Ma et al. (2010); the final fit parameters are given in Table 5.

The imaged pores were assumed to be embedded within a single crystal oriented so that the fastest growth direction ([111] for the fcc matrix) was aligned with the build direction (the Z-direction in the figures). This is consistent with experimental experience which suggests that grains in IN718 are much larger than the pores and preferentially orientated (Parimi et al., 2014; Moussaoui et al., 2018). However, this assumption could easily be refined in future work, e.g. to include grains in the microscale representation, if more information for local grain orientation is forthcoming.

A snapshot of the thermal response for the part being built under one of the scan strategies and processing parameter sets is shown as contours of temperature in Fig. 10, as an example of the thermal prediction. This thermal prediction progresses through the full building process for this specimen.

Forty different virtual test specimens, each a different instantiation, were simulated. Each had a slightly different spatial configuration of defects because of the randomness introduced in the microstructure selection phase. Thus, the estimated fatigue life varied between specimens.

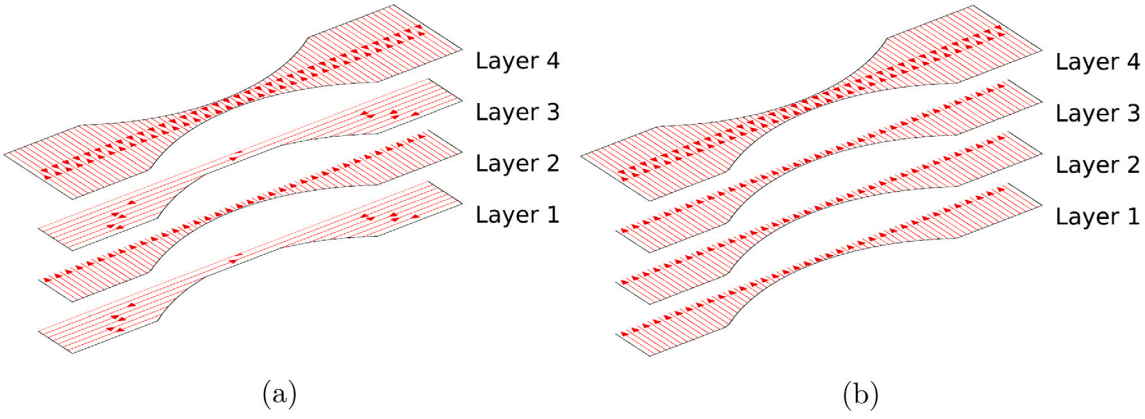

Fig. 9. Schematics of the (a) zig-zag and (b) unidirectional scan strategies.

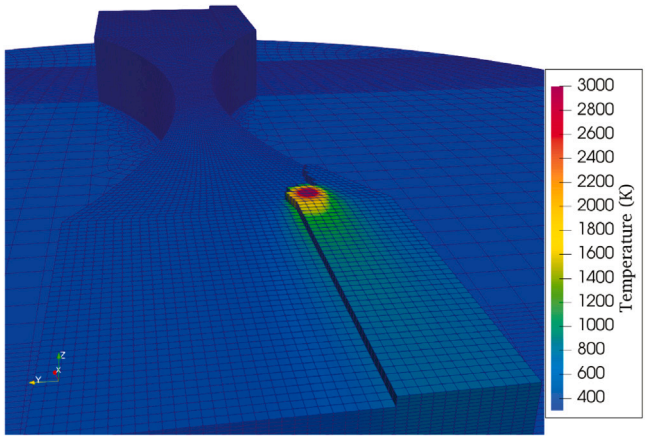

Fig. 10. The continuous radius fatigue test specimen, showing the thermal processing prediction partway through the build. The peak temperature and temperatures gradients seem physically reasonable, appearing similar to those shown in Bennett et al. (2017).

Each element in the macroscale specimen is represented by an image of a void, represented by a voxel mesh from the database of microstructures. Thus, each specimen has about 65 billion voxels across all the microstructures. Direct simulation of a system this large is intractably computationally expensive except, perhaps, on some of the very largest computers, not practical for designers or practitioners (see for example Rodgers et al., 2018). Using CPSCA at the microscale with 16 clusters in the matrix phase and four in the pore phase reduces the computational expense, making it possible to run the simulation using a modern workstation computer (or one node of a cluster computer, in this case). The microscale simulation with CPSCA for each simulation takes about nine hours using 36 cores in parallel on Intel Xeon Skylake 6140 CPUs at 2.9 GHz clock speed (or 324 CPU hours). The macroscale solution only takes a few minutes on 72 of the same CPUs. This run time puts design iteration within the realm of possibility for individuals or small companies.

The resulting microstructure-based fatigue life predictions are shown in Fig. 11. The plotted points fall on a strain-life curve showing the overall minimum estimated life for five instantiations of specimens for each of three different load amplitudes for two different processing conditions. Changing processing conditions changes the solidification cooling rate at each point, and thus changes the possible microstructures available to represent that point, which in the end changes predicted failure site and number of cycles to failure.

The results in Fig. 11 demonstrate the key features of this method. The contour plots of the gage sections report an estimated number of cycles required to cause fatigue crack initiation at each macroscale point in the fatigue specimen; at any given macroscale point, the microstructure is different between different instantiations (Specimen A versus Specimen B at the top of Fig. 11), which results in different contours plots. Comparing the microstructures between Specimen A and Specimen B provides the reason behind this difference: features with higher fatigue potency might, by random chance, occur at the point of highest strain concentration in one instantiation but not another. This is similar to behavior seen in physical testing (Gong et al., 2015; Johnson et al., 2017; Gribbin et al., 2016; Sheridan et al., 2018). Note that because of the relatively limited number of microstructures in the database use for this demonstration, one particular microstructure tends to result in failure throughout the specimens (see Fig. 11).

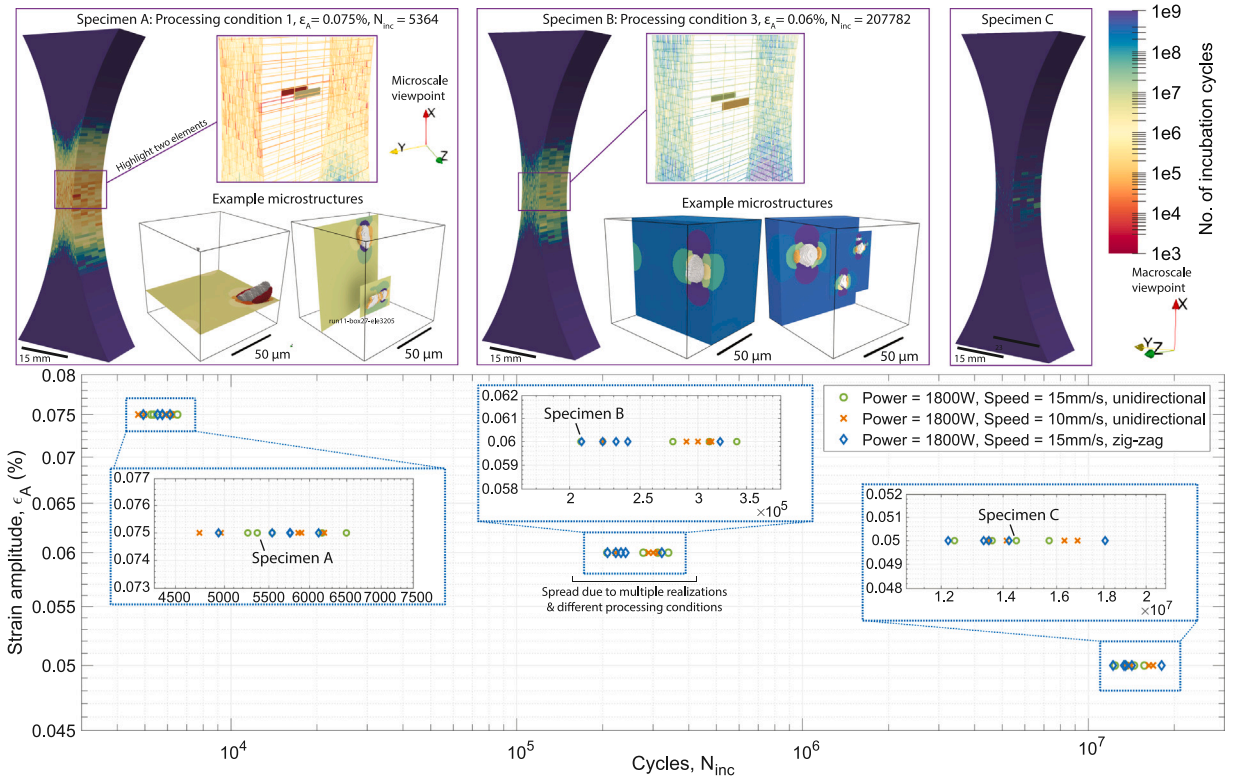

Fig. 11. Estimated fatigue crack incubation life for multiple instantiations, with three different applied strain amplitudes. Note that spread in the x-axes represents run-to-run variability resulting from different microstructures selected for different runs. Also notice that at the two lower strain amplitudes, the zig-zag scan strategy, which has overall higher void volume fraction due to an overall lower (closer to zero) solidification cooling rate, has slightly lower fatigue life.

A comparison of these results to similar tests conducted by Johnson et al. (2017) for DED IN718 shows similar trends for fatigue life, although the applied strain levels are quite different. However, the specimen geometries are different: Johnson et al. uses a constant cross-section geometry, whereas our specimens have a dogbone geometry. The dogbone geometry results in a strain concentration factor of about ten (see Fig. 6), which when used to compute an effective strain for comparison with Johnson et al. provides relatively similar results, as shown in Fig. 12. Even when using this effective strain, slope of the two strain-life plots remain slightly different. This difference can likely be explained by considering that the FIP equation used in these predictions is based on wrought material data at relatively high cycle regime, which has a relatively low slope. There are factors that may decrease the high cycle fatigue life for AM IN718 which are not accounted for: Johnson et al. suggests that hard particles (e.g. δ-phase) could be a driving factor in the high cycle behavior (Johnson et al., 2017); such hard particles were not included in the present model. Promisingly, the range of the fatigue data is similar between the model and experiment. We expect that more accurate predictions can be made given better fitting data, if such data were made available to us. To test this hypothesis, we set the two FIP fitting parameters to $\gamma_f = 3.7$ and $c = -0.85$, and observe that the experimental results are reproduced nearly exactly.

3.2. Fracture initiation prediction

A compact tension specimen conforming to the ASTM E399 standard test geometry was simulated using this framework. The goals of this model are twofold: (1) to show that the fracture initiation point is captured, and (2) to demonstrate that by using variable microstructures, predicted onset of fracture will vary and thus we can hope to predict and perhaps control fracture onset in AM builds.

A thermal simulation of the build was conducted with the Z-direction along the build axis with a very fine mesh; the thermal analysis took 107.0 CPU hours on 24 of the 2.3 GHz CPUs. A converged mesh, with respect to macroscale stress profiles, for the mechanical simulation was used for the stress analysis, as shown in Fig. 13(a). There are two elements per build layer, reduced from five in the thermal mesh. A symmetry boundary condition was applied to the +Z face, and free boundary conditions were applied on all other surfaces. Two rigid cylinders were used as pins with predefined displacement in the Y-direction and simple contact to achieve bulk-scale Mode-I-type deformation, roughly modeling common quasistatic experimental conditions (the pins are not shown in the figures). An initially-blunted crack with root radius 0.254 mm was considered, which is more easily processed in the thermal simulation than a geometry with a sharp crack tip root. A sharp-tip initial configuration is unnecessary, as things like

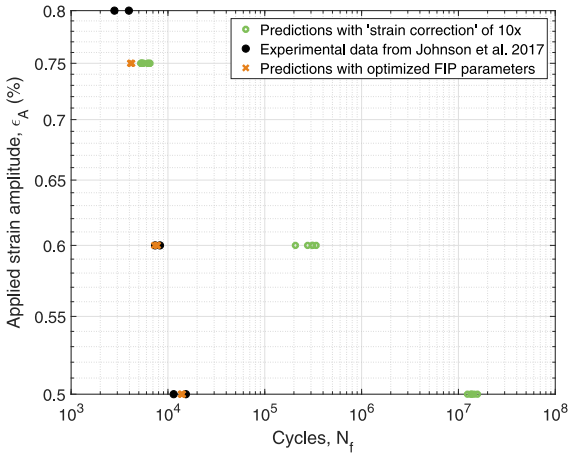

Fig. 12. A comparison between predictions (green circles) for parameter set 1 with a "correction factor" to account for strain concentration from the dogbone geometry and entirely independent fatigue measurements of Johnson et al. (2017). The differences are likely because the FIP for the fatigue data was fit to wrought material fatigue life and further factors that could be important in the high cycle regime were not included in the present model. By changing only the fit parameters for FIP, the experimental results can be reproduced, indicating they may be the driving difference. (For interpretation of the references to color in this figure legend, the reader is referred to the web version of this article.)

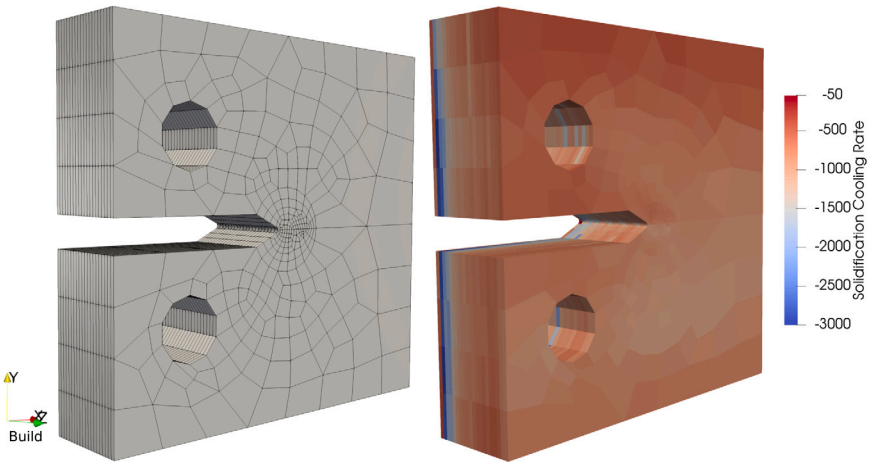

Fig. 13. Compact tension geometry example: (a) mesh, pin loading from rigid pins excluded from this visualization (b) solidification cooling rate prediction.

fracture toughness or propagation are not being measured. The point of the model is rather to highlight the variable nature of the fracture initiation process given the underlying microscale variability. The same database of microscale voxel meshes of imaged porosity were used as in the fatigue example.

Because of the larger deformations involved here compared to those in the fatigue problem, the two-way concurrent coupling method was used for the mechanical solver. A rigorous derivation and details regarding the implementation of the concurrent scheme for two-scale coupling (used here) and the generalization to many-scale coupling is provided in Yu (2019) and Yu et al. (2019). Fracture initiation was predicted using the experimentally-determined failure surface described in Appendix E.

Descriptive statistics regarding the initial microstructural configuration are shown in contour plots at the macroscale and collected in histograms in Fig. 14. Some example statistics that describe the microstructures within a given instance are shown in Fig. 14. Nearest neighbor distance may be of interest in future, because void spacing may be related to fracture behavior, although this was not used in the current model as a selection criterion. From a design perspective, a parametric study of the impact of any of the factors (e.g. using prescribed microstructural geometry) would be possible in the current framework as well. Using FE-CPSCA, this takes about 23 h on 108 of the 2.9 GHz CPUs (or 2484 CPU hours); notice that because the two-way coupling is required this is more expensive than the fatigue example. This is predominately because the time steps have to be much smaller than for the fatigue example to ensure convergence, but also because the second stage of the SCA prediction may be called multiple times during each timestep to for the macroscale time stepping scheme to converge, whereas this is not necessary in the one-way coupling used for the fatigue example.

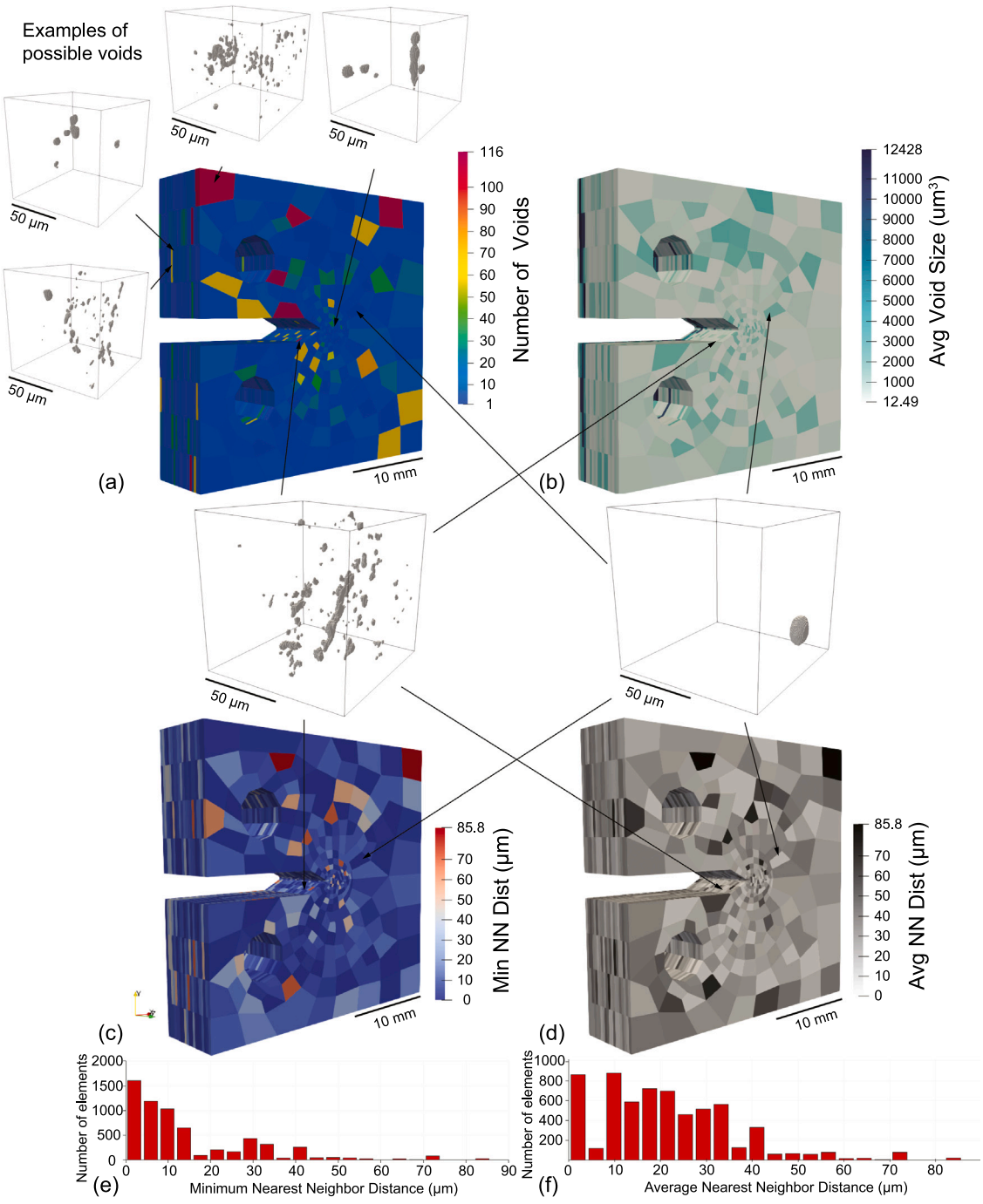

Fig. 14. One instantiation of the fracture model. Contour plots of (a) number of pores in the microscale for each element, (b) average pore size for within the microscale, (c) minimum nearest neighbor distance, (d) average nearest neighbor distance (a value of zero in (c) and (d) indicates only one pore is present); (e) histogram of minimum nearest neighbor distance, (f) histogram of average nearest neighbor distance.

Fig. 15 shows the results from this fracture initiation simulation. Subset (F) shows the deformed configuration of the compact tension specimen with YY direction stress contours after 2.896 mm of total displacement of the pins in the Y-direction. Note that some elements at the crack tip have failed, and as a result no longer hold stress (near the center of the blunted crack region). The contour plot in Fig. 15(G) shows the number of failed cluster in each sub-scale mesh, tracking the progress of damage; several specific elements are numbered in Fig. 15(C), and the corresponding microstructures are shown in Fig. 15(A–E), colored by the YY component of the PK1 stress. The microstructures in Fig. 15(A), (B), (D), and (E) have failed regions and thus hold lower load than

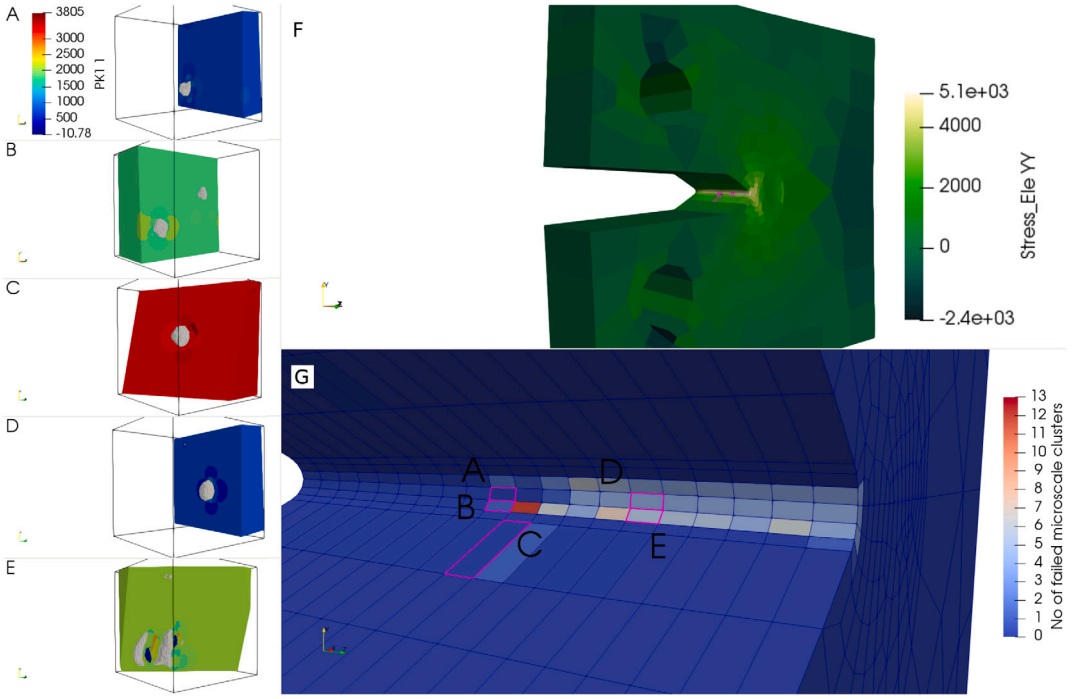

Fig. 15. Concurrent multiscale model for fracture initiation with varying microstructures. (A–E) PK1 YY (or 1 in Voigt notation) stress contours of the microscales at the elements highlighted in (G); note that some pores interact and cause larger failed zones or increase stresses; (F) contours of stress in the YY direction after fracture has begun, note "failed" elements with decreased stresses at crack tip; (G) map showing the prevalence of failure, the color shows the number of clusters failed at the microscale, 0 = no failures, 20 = completely failed. The variation of fracture potency depends on local deformation and the microstructure expressed at that material point.

(C), which has not had any clusters in the microstructure fail. As with the fatigue example, different instances of the model result in different fracture locations.

4. Discussion and findings

The novel contributions of this work is the use of data-driven multiscale modeling to capture the effect on mechanical performance of random, as well as potentially systematic, and processing-history based changes in microstructure. Although currently not designed to represent one particular AM system, the model includes a mix of deterministic and random factors, such that the results vary between different runs with the same build conditions and between build conditions. In some respects, this might be classified as a digital twin, while a focus on other aspects of the model might align in more closely with an uncertainty estimation, or quantification of uncertainty. In either case, the contribution is a mechanistic method that directly computes the effect of a heterogeneous distribution of different defects on mechanical performance metrics of interest such as fatigue life and fracture initiation potency. This is particularly relevant to additively manufactured materials, because such defects are inhomogeneously distributed, confounding typical representative volume or other homogenization type methods, and in some cases limit the strength of the material, e.g. are responsible for reduced fatigue lives. Thus, we have demonstrated the method using images of voids from AM metal and simulated processing conditions.

More conventional, and simpler, methods such as the critical or rogue flaw approaches most often assume that a single most dangerous defect or flaw exists and will cause failure. On this basis, expected life can be defined in terms of the highest stress location in combination with the largest, or worst, defect. This usually provides a suitably conservative estimate for highly safety critical applications. However, for AM, selecting what the worst defect is may not necessarily be obvious. Moreover, enforcing a conservative estimate without being able to adjust the method to represent varying levels of confidence may not be desirable for AM applications were weight and efficiency matter.

In a practical design for fatigue setting, the proposed model would provide a probabilistic paradigm, while also being sensitive to critical defects. Although unlikely to replace safe life design using the critical defect method for highly safety critical components due to its added complexity, the current method represents a mechanistic approach to incorporate statistical variability and directly represent different possible defects any of which may be the critical one depending on the specific stress states and geometries involved. The method might be thought of as a generalization of the critical defect methodology. Consider a limiting case that a single defect is included in the model, i.e., the database has a single entry that is selected *a priori*. The predicted fatigue life would be the same as a "critical defect in the critical location" analysis using the same FIP framework, assuming the selected defect is the

Table 6
Selection of key parameters describing the contents of the offline database and the computational savings of the reduced order model.

No. of sub-images	320
Void volume fraction range	0.01% to 4.5%
Pore sizes	About $2\,\mu m^3$ to $4.2 \times 10^4\ \mu m^3$
Grid size (voxel mesh)	$150 \times 150 \times 150$
No. of voxels per image	3375000
Voxel edge length	$0.65\,\mu m$
Volume of each image	$9.27 \times 10^5\ \mu m^3$
No. of clusters per image	20
Clusters based on	K-means on elastic strain

Table 7
Table describing the most relevant numerical details of the fatigue problem.

Macroscale solver	Implicit FE
Maximum timestep	0.1 s
No. of macroscale elements	19020
No. of macroscale nodes	25010
Macroscale element type	Reduced integration hex
Hourglass control type	"Enhanced"
Total strain rate	$1 \times 10^{-4}\ s^{-1}$
Deformation profile	Cyclic triangle waveform
Macroscale material model	Johnson–Cook (macroscale is elastic)
Microscale solver	CPSCA (deformation BCs)
Total no. of voxels (micro)	$19020 \times 150^3 = 64.2 \times 10^9$
Total no. of clusters (micro)	380400
Concurrent coupling technique	One-way
Compute time (36 CPUs)	About 360 CPU hours

Table 8
Computational details of the fracture initiation problem.

Macroscale solver	Implicit FE
Static stabilization parameter	0.0002
Maximum timestep	0.001 s
No. of macroscale elements	6220
No. of macroscale nodes	7245
Macroscale element type	Reduced integration hex
Hourglass control type	"Enhanced"
Contact (for pin loading)	Hard pressure overclosure
Total displacement rate	0.4 mm/s
Displacement profile	Monotonic opening
Macroscale material model	Concurrent multiscale
Concurrent coupling technique	Two-way
Number of macroscale state variables	1543
Microscale solver	CPSCA (as user material at microscale)
Total no. of voxels (micro)	$6220 \times 150^3 = 64.2 \times 10^9$
Total no. of clusters (micro)	124400
Total no. of pores (micro)	54655 for the realization shown
Compute time (on 108 CPUs)	2484 CPU hours

critical defect, and the critical location is correctly determined for the critical defect analysis. This could benefit settings in which design for mean performance is more appropriate, or in topologically optimized geometries with highly variable stress states and geometry.

There are a number of facets that warrant further discussion and continuing refinement. One important aspect of the model is the efficiency of the reduced order model, and the enabling effect this has upon the simulation process. An overview of the complexity of the different models constructed here: the scale of the problem and dimension reduction achieved, is shown in Table 6 for database generation step, Table 7 for the fatigue problem and Table 8 for the fracture problem. The scale of the problem at the part scale makes what we have achieved – direct, mechanistic representation of microstructures – unique given the limited computational effort expended.

The method currently makes use of descriptors that connect processing conditions to selection of a microstructure that represents that condition. One of the simplest possible approximations is made here, but further refinement is possible. The thermal model and microstructure descriptors could be enhance, for example. An improved metric or relationship, perhaps requiring a thermal/multiphase flow model with more advanced capabilities, would allow the system to more accurately capture physical reality. For example, a measure of distribution of porosity within each microstructure (i.e. if it is one large pore or many small ones) such as nearest neighbor distance might be used in addition to V_f if such information were available from the process model;

another option would be to include neighborhood information, e.g., with a two-point correlation function as has been done in classical literature for elastic homogenization problems.

The microstructures used here do not explicitly capture surface effects for the microstructural fatigue behavior. For example, a pore on the microscale near the surface of the part might have an larger impact on fatigue performance than that same pore in the bulk material. While the macroscale effects of the boundaries are naturally included, this small scale interaction is a matter of ongoing work. Some authors, Yadollahi and Shamsaei (2017), suggest that there is limited change in overall fatigue life, up to the high-cycle limit (runout), for as-built versus machine-finished specimens; this may indicate the assumption made here is reasonable, but this is controversial as other authors suggest that the lower surface roughness of machine-finished specimens increases fatigue life (Gockel et al., 2019).

In addition, the database used here contained only 320 possible microstructures. Thus, each microstructure was repeated many times throughout a given macroscale. This implies that the likelihood of the critical flaw (or worst-case microstructure) occurring within the most highly stress area of the specimens is quite high. This artificially decreases the observed fluctuations in fatigue life. Some relationship between the number of sub-scale microstructures required in the database and either the range of SCR or the region of the critical volume for failure could be developed to support this framework. Generally, the test of an adequately-sized database might involve comparing macroscale measures of predictiveness between standard experiments and models with an increasing number of microstructures until the values and variability of the simulated results were within those of the experiments. Such parameters could be probability of failure curves in fatigue or displacement at failure in fracture, for example. Ideally, a fixed distribution of microstructures throughout the range of thermal conditions would be maintained so as to avoid adding another biasing factor when changing the database size.

A simplifying assumption for the grain structure (single crystal at the microscale) was also used for this demonstration; however, we could add a step that either predicts the grain structure from the thermal history, as we demonstrated in Yan et al. (2018a), or derives a grain structure from experiments if more of that data were available. Prior modeling results, Yan et al. (2018a) and Cheng et al. (2020), indicate that grains generated this way could substantially impact predicted plastic deformations and fatigue lives when used in concert with image-based pore geometries.

An implicit assumption of all the images used here is that the hatch spacing and laser power were appropriate to avoid lack-of-fusion defects between tracks. Because, as one will recall, the images used to make the database came from single-track, thin-wall builds, where no between-track porosity would be possible. This assumption could easily be relaxed by including images of pores from more general build conditions in the database. Furthermore, all volumes are assigned such that the build direction in the simulation aligns with the build direction of the imaged material. Changing the orientation of the images would alter the direction of load with respect to the voids/defect clusters, and thus potentially alter the fatigue and fracture behavior.

Although for this demonstration we assume that pores always occur and dominate the failure response, this is not a necessary assumption of the method — given sufficient characterization data of the processed material, many classes of microstructure might be used with this framework. For example, grain and pore combinations could easily be used (an implementation exists) to account for the effects of grain boundaries and polycrystalline mechanics in general, as mentioned above. Another possible example would be to include a description of the dislocation cells or overall density (possibly much more prominent in AM materials than conventional materials Yan et al., 2018b), or other phases such as strengthening precipitates.

Development of a benchmark for fatigue and fracture prediction in AM would support these modeling efforts. Currently, conflicting reports of the influence of AM, versus conventional processing, on the fatigue properties of metals exist. For example, compare DED material tested by Johnson et al. (2017) and selective laser melting (SLM) material reported in Witkin et al. (2019). This can in part be attributed to the wide range of materials, but also to a range of build processes and choices made by machine operators. This makes it challenging to develop reliable, generalizable models. In order to calibrate the models fully, in addition to the material properties some data regarding fatigue life is required to compute the fitting factors in the FIP. For the failure model, a local measure of failure potency is needed — in this case, we used failure surface in terms of effective plastic strain at a given stress triaxiality and Lode angle. Experiments that deduce this relationship are necessary. If further developments include fracture progression in addition to initiation, some measure of separation energy or another factor related to the ductile failure may be required as well (currently, a simple assumption for post-failure behavior is used to avoid this).

Finally, although the various tools have been validated, experimental verification of the prediction results is ongoing. As shown for the fatigue results, access to data with which to fit the FIP predictions is critical for an accurate prediction of fatigue life. Fatigue and fracture experiments that are directly comparable with the predictions made in these demonstrations are under development, and we hope will improve accuracy and provide more direct comparisons. Although some experimental results in the literature (Gong et al., 2015; Shamsaei et al., 2015, or Beretta and Romano, 2017) might give some confidence that the trends we identify are reasonable, more specific comparisons would require specifically designed experiments.

5. Summary and conclusions

We have presented a method that exploits computationally efficient micromechanics techniques to perform Monte Carlo-style sampling with numerical experiments, using XCT images of real AM microscale pores. The specific microscale solutions are derived from a cluster-based solution of the Lippmann–Schwinger equation, and involve the prediction of fatigue life using crystal plasticity and a fatigue indicating parameter. A database of possible microscale geometries is developed from 3D imaging experiments. These geometries are related to AM processing conditions through the solidification cooling rate, and a process- and microstructure dependent, stochastic prediction of fatigue life and fracture initiation are achieved with reasonable computational expense.

There are two key innovations here. First, the microstructure varies spatially within a part, specifically according to a process model. This is unusual in concurrent multiscale modeling approaches. This means that fluctuations in performance can be captured; which may enable more realistic modeling of the variability that occurs due to localized material processing such as AM than what might be accomplished with metamodels or other ways of capturing variability. This is a fundamental contribution to the field, introducing an innovative mechanistic microstructural volume element-based computational framework that moves beyond the current representative volume element paradigm. Second, experimental 3D images of the microstructures of interest are used directly. Use an image database for concurrent multiscale modeling does not, to the best of our knowledge, appear elsewhere in the literature. This provides the variability needed for the first innovation and involves higher fidelity material representation, because simplified geometric representation commonly used for multiscale, reduced order, or homogenization type problems are avoided. The method can also be used to select microstructures that result in greater fatigue life or fracture resistance, with direct, physical representation of the underlying mechanics that control the process.

One possible future direction is simulating the effects of functionally graded or otherwise designed or planned heterogeneity on overall or local mechanical performance. Several papers in recent years have claimed to be able to achieve some control of microstructure by controlling heat input and scan strategy or adding other mechanisms to the build processes such as bulk heating/cooling or vibration. For example, Dehoff et al. (2015) showed that site specific columnar versus equiaxed growth can be achieved. While this was for a different material and process, it shows that there may be hope in controlling the local properties through specific choices in the processing history. This control may also be possible for defects, at least in some capacity, e.g. by avoiding scan strategies that put a higher chance of defects at a fatigue- or fracture-critical location. What we have shown in a method capable of capturing the impact of these kinds of site-specific microstructure factors (specifically we have studied voids, although the method is not limited to single-crystals and voids alone).

The complex method here could also be simplified or used to inform a simplified method in several ways. For example, the database could be constructed with representative classes of defects, rather than directly from images, reducing the experimental requirements of the method. Alternatively, learnings from this method could be used to inform and develop simplified modeling approaches that empirically implement similar ideas in a more tractable environment, such as by using similarly varying physically-inspired evolution equations in a continuum damage mechanics framework, rather than directly representing images of defects and crystallographic effects.

Another possible example is by integrating our method with microstructure-aware topology optimization, such as Li et al. (2019a). Finally, while the relationship shown here to connect the outputs of the processing model with microstructures, using the solidification cooling rate, is tenuous and not well validated, in future we can easily replace this with a validated mechanistic or physical relationship, should a better one become available.

CRediT authorship contribution statement

Orion L. Kafka: Conceptualization, Methodology, Software, Validation, Investigation, Resources, Data curation, Writing - original draft, Writing - review & editing, Project administration, Visualization, Supervision, Funding acquisition. **Kevontrez K. Jones:** Software, Visualization, Investigation Writing - original draft, Writing - review & editing, Specializing in thermal analysis. **Cheng Yu:** Software, Visualization, Investigation, Writing - review & editing, Specializing in micromechanical analysis. **Puikei Cheng:** Software, Investigation, Data curation, Writing - original draft, Specializing in process-structure relationship and database construction. **Wing Kam Liu:** Supervision, Resources, Writing - review & editing, Funding acquisition.

Declaration of competing interest

The authors declare that they have no known competing financial interests or personal relationships that could have appeared to influence the work reported in this paper.

Acknowledgments

The experimental X-ray imaging was conducted via a user-access proposal with the help of Xianghui Xiao of Beamline 2BM at the Advanced Photon Source, a U.S. Department of Energy (DOE) Office of Science User Facility operated for the DOE Office of Science by Argonne National Laboratory, United States under Contract No. DE-AC02-06CH11357. The preliminary experimental work also made use of the MatCI Facility which receives support from the MRSEC Program (NSF DMR-1720139) of the Materials Research Center at Northwestern University. OLK and WKL were funded by the National Science Foundation's Mechanics of Materials and Structures (MOMS) program under the Grant No. MOMS/CMMI-1762035. OLK also acknowledges the support of the NSF Graduate Research Fellowship, United States under Grant No. DGE-1324585a. WKL also thanks the Center for Hierarchical Materials Design (CHiMaD), United States under Grant Nos. 70NANB13Hl94, 70NANB14H012, and CHiMaD Phase 2, United States under 70NANB19H005.

Appendix A. Thermal model equations

The governing heat transfer energy balance to be solved is:

$$\frac{\partial \rho c_p}{\partial t} = \frac{\partial}{\partial x_i}\left(k\frac{\partial T}{\partial x_i}\right) \tag{A.1}$$

where ρ is the material density, c_p is the specific heat, t is the time, x_i are the spatial coordinates, k is the conductivity of the material, T is the temperature. Note that this model only capture heat conduction within the material. While this is a simplification, prior studies such as that by Heigel et al. (2015) show that conduction is the dominant mode of heat transfer in DED.

A heat source Q is used to represent a moving laser. It is modeled using a moving boundary condition to apply a surface flux described by the Gaussian distribution:

$$Q = \frac{2P\eta}{\pi R_b^2}\exp\left(\frac{-2\left(x^2+y^2+z^2\right)}{R_b^2}\right) \tag{A.2}$$

where P is the power of the laser, η is an absorptivity factor to limit the amount of energy absorbed by the material from the laser which was taken to be 30%, and R_b is the radius of the laser. The variables x, y, and z are local coordinates of the laser. Heat loss on the dynamic free surfaces of the model is simulated though a combination of convection and radiation. Convective heat loss is defined by

$$q_{conv} = h_c\left(T - T_\infty\right) \tag{A.3}$$

where h_c is a convection coefficient and it was taken to be 10 $\frac{W}{m^2 K}$, T is the surface temperatures, and T_∞ is the far-field (ambient) temperature. Radiative heat loss is defined using the Stefan–Boltzmann law, given by

$$q_{rad} = \sigma_s \epsilon\left(T^4 - T_\infty^4\right) \tag{A.4}$$

where σ_s is the Stefan–Boltzmann constant and ϵ is the surface emissivity of the material, which was taken to be 40%. Eqs. (A.1), (A.2), (A.3), and (A.4) are implemented within a custom finite element code optimized to solve these equations efficiently.

Appendix B. Relate thermal model outputs and defects

Relating process model results to material defects is an developing field of research, and constructing such a relationship is not the focus of this work. Thus, we simply use the exponential relationship between solidification cooling rate (SCR) and void volume fraction (V_f) identified by Wolff et al. (2017) as

$$V_{frac} = Ae^{-(B)(SCR)}. \tag{B.1}$$

The parameters in Eq. (B.1) are fit to thermal and porosity data from two thin wall DED builds as $A = 0.0047$ and $B = -0.0011$ and 95% confidence bounds of (0.00385, 0.005537) and (−0.00194, −0.0001895) respectively. For the current set of AM builds we were unable to find a more highly correlated relationship (with a closer interval) to predict V_f from thermal results, which may indicate a limitation in general for the such an empirical correlation.

Although further research is needed to improve the correlation it suffices for the purposes of this study, which focuses upon the structure-properties relationship enabled by image-based reduced order modeling. Similar relationships, where factors that govern thermal history are related to porosity, are made elsewhere e.g. Kasperovich and Hausmann (2015), and could be substituted in practice as needed or if a much more convincing relationship is identified in future work.

Appendix C. Microstructure selection algorithm

The step-by-step process for selecting each microstructure given all necessary information is as follows.

Box 1: Algorithm for microstructure selection

1. Initial data
   (a) Load SCR data (on the mesh defined for the thermal simulation)
   (b) Load stress mesh (the mesh used for stress analysis at the macroscale)
   (c) Load microscale database
2. For each element in stress mesh:
   (a) Compute average SCR for element
   (b) Compute volume fraction V_f from SCR with Eq. (B.1)
   (c) Find all microstructures in database within ±20% of that V_f
   (d) Pick 1 microstructure at random from the available microstructures (those within 20%)
   (e) Otherwise, if no microstructure are within ±20%:
      i. if V_f > maximum V_f: pick 1 microstructure at random from 5 special "large V_f" options
      ii. if V_f < minimum V_f: pick 1 microstructure at random from 5 special "small V_f" options

After each element has a microscale assigned, begin two-scale modeling:

- If one-way model: solve response of each microscale with pre-computed stress-history at each point
- If two-way model: in macroscale user material, load in all microscale data, store in an element-by-element 2D and 3D arrays and access each elementÃćâĆňâĎćs data as needed (e.g. V_f is stored with one entry per phase per element in a 2D array $v_f(nP, nElem)$, where nP is the number of clusters and $nElem$ is the number of elements in the stress mesh)

Appendix D. Lippmann–Schwinger equation for reduced order modeling

This method has been described in detail elsewhere; the interested reader is directed to Kafka et al. (2018), Shakoor et al. (2018) and Yu et al. (2019) for further information. If we define the equilibrium mechanical response problem in a finite strain setting in the undeformed configuration, as Yu et al. (2019), we arrive at:

$$\begin{cases} \frac{\partial \mathbf{P}}{\partial \mathbf{X}} = \mathbf{0}, \forall \mathbf{X} \in \boldsymbol{\Omega}, \\ \mathbf{F} = \frac{\partial \mathbf{u}}{\partial \mathbf{X}}, \forall \mathbf{X} \in \boldsymbol{\Omega}, \\ \frac{1}{|\boldsymbol{\Omega}|} \int_{\boldsymbol{\Omega}} \mathbf{F} \mathrm{d}\boldsymbol{\Omega} = \mathbf{F}^0, \end{cases} \tag{D.1}$$

where $\mathbf{P}$ is the first Piola–Kirchhoff stress, $\mathbf{F}$ is the deformation gradient, $\mathbf{u}$ is the displacement, and $\mathbf{X}$ is a material point within domain $\boldsymbol{\Omega}$. Similarly, this can be written in small strain, where the Cauchy stress and strain are used as fundamental variables, as in Kafka et al. (2018). Following Yu et al. (2019), if we assume periodic boundary conditions and far-field pure deformation loading conditions, Eq. (D.1) can be shown to be equivalent to the Lippmann–Schwinger equation given by:

$$\mathbf{F}(\mathbf{X}) + \boldsymbol{\Gamma}^0 * \left(\mathbf{P}(\mathbf{X}) - \mathbf{C}^0 : \mathbf{F}(\mathbf{X})\right) - \mathbf{F}^0 = \mathbf{0}, \forall \mathbf{X} \in \boldsymbol{\Omega} \tag{D.2}$$

where the 4th order Green's operator, $\boldsymbol{\Gamma}^0$, is associated with an arbitrary reference stiffness tensor $\mathbf{C}^0$, and $*$ denotes the convolution operation.

To achieve a reduced order approximation of the solution, we use an arbitrary set of sub-domains within the full domain, rather than the original mesh. To define the sub-domains, or *clusters*, that achieve high prediction accuracy, clustering is based on a training dataset. Here, we choose either the strain concentration tensor, $\mathbf{A}^m$ defined by $\boldsymbol{\epsilon}^m(\mathbf{X}) = \mathbf{A}^m(\mathbf{X}) : \bar{\boldsymbol{\epsilon}},\ \mathbf{X} \in \boldsymbol{\Omega}$ (as in Kafka et al., 2018, where $\boldsymbol{\epsilon}^m(\mathbf{X})$ is the local strain at point $\mathbf{X}$ and $\bar{\boldsymbol{\epsilon}}$ is the remote applied strain) or, if a finite deformation setting is used, the deformation concentration tensor , as defined by $\mathbf{A}(\mathbf{X}) = \frac{\partial \mathbf{F}(\mathbf{X})}{\partial \mathbf{F}^0}, \forall \mathbf{X} \in \boldsymbol{\Omega}$ (as in Yu et al., 2019). For each phase in the material, voxels with similar $\mathbf{A}^m$ are assigned to one of a predetermined number of clusters $I = 1 \ldots k$ using k-means clustering (MacQueen et al., 1967).

Eq. (D.2) can be defined cluster-wise and applied to the cluster data, where the solution variables are assumed to be constant in an given cluster. In the finite deformation formulation, derived in Yu et al. (2019) and given as:

$$\mathbf{F}^I + \sum_{J=1}^{N_c} \mathbf{D}^{IJ} : \left[\mathbf{P}^J - \mathbf{C}^0 : \mathbf{F}^J\right] - \mathbf{F}^0 = \mathbf{0}, \text{with } I = 1, \ldots, N_c, \tag{D.3}$$

where $\mathbf{F}^J$ is the deformation throughout cluster J, $\mathbf{P}^J$ is the stress in that cluster, and N_c is the total number of clusters. The so-called interaction tensor, $\mathbf{D}^{IJ}$, is defined in Eq. (9) of Yu et al. (2019). The cluster-wise Lippmann–Schwinger equation given in Eq. (D.3) is solved using the techniques described in Yu et al. (2019).

Appendix E. Failure surface for fracture initiation

To estimate fracture initiation locally within each cluster at the microscale, we choose to measure the local plastic strain, and compare that value to a "critical failure strain" reported from measurements of fracture surfaces of wrought IN718 in a thesis by Ressa (2015) in terms of the Lode angle parameter and stress triaxiality at failure (T_F). The critical failure strain was fit with a polynomial surface to experimental data points, as given by

$$\begin{aligned} \epsilon^p_{critical} &= 0.6975 - 0.02614(\bar{\theta}) - 0.8662(T_F) \\ &\quad - 0.03889(\bar{\theta})^2 - 0.1643(\bar{\theta})(T_F) + 0.4206(T_F)^2 \\ &\quad + 0.4206(T_F)^3 - 0.1934(\bar{\theta})^2(T_F) + 0.249(\bar{\theta})(T_F)^2 \end{aligned} \tag{E.1}$$

where $\bar{\theta}$ is the Lode angle parameter and T_F is the triaxiality. The general construction for Eq. (E.1) is suggested by Ressa (2015), although this fit to the data was conducted in the present study. A simple weakening factor was further applied; after a microscale cluster is marked as "failed" according to its stress state, it remains failed and for every subsequent increment its stiffness is homogeneously reduced by a factor 5% greater than the previous factor starting at zero and increasing until 95%, effective removing its load-bearing capability shortly after failure. This "progressive" failure helps the computational stability of the microscale solver, but eventually (once enough elements fail) on the macroscale the implicit FEA encounters convergence difficulties and is halted.

References

Amanov, A., Pyun, Y.-S., Kim, J.-H., Suh, C.-M., Cho, I.-S., Kim, H.-D., Wang, Q., Khan, M.K., 2015. Ultrasonic fatigue performance of high temperature structural material Inconel 718 alloys at high temperature after UNSM treatment. Fatigue Fract. Eng. Mater. Struct. 38 (11), 1266–1273. http://dx.doi.org/10.1111/ffe.12330.

Antonysamy, A.A., Meyer, J., Prangnell, P.B., 2013. Effect of build geometry on the Beta-grain structure and texture in additive manufacture of Ti6Al4V by selective electron beam melting. Mater. Charact. 84, 153–168. http://dx.doi.org/10.1016/j.matchar.2013.07.012.

ASTM, 2015. Practice for conducting force controlled constant amplitude axial fatigue tests of metallic materials. pp. 1–6, E466-15.

Belan, J., 2015. High frequency fatigue test of IN 718 alloy–microstructure and fractography evaluation. Metalurgija 54 (1), 59–62. http://dx.doi.org/10.4028/www.scientific.net/KEM.635.9.

Belytschko, T., Liu, W.K., Moran, B., Elkhodary, K., 2013. Nonlinear Finite Elements for Continua and Structures. John Wiley & Sons.

Bennett, J.L., Kafka, O.L., Liao, H., Wolff, S.J., Yu, C., Cheng, P., Hyatt, G., Ehmann, K., Cao, J., 2018. Cooling rate effect on tensile strength of laser deposited Inconel 718. In: Procedia Manuf., Vol. 26. pp. 912–919. http://dx.doi.org/10.1016/j.promfg.2018.07.118.

Bennett, J.L., Wolff, S.J., Hyatt, G., Ehmann, K., Cao, J., 2017. Thermal effect on clad dimension for laser deposited Inconel 718. J. Manuf. Process. 28, 550–557. http://dx.doi.org/10.1016/j.jmapro.2017.04.024.

Beretta, S., Romano, S., 2017. A comparison of fatigue strength sensitivity to defects for materials manufactured by AM or traditional processes. Int. J. Fatigue 94, 178–191. http://dx.doi.org/10.1016/j.ijfatigue.2016.06.020.

Carroll, B.E., Palmer, T.A., Beese, A.M., 2015. Anisotropic tensile behavior of Ti-6Al-4V components fabricated with directed energy deposition additive manufacturing. Acta Mater. 87, 309–320. http://dx.doi.org/10.1016/j.actamat.2014.12.054.

Chen, Q., Kawagoishi, N., Wang, Q.Y., Yan, N., Ono, T., Hashiguchi, G., 2005. Small crack behavior and fracture of nickel-based superalloy under ultrasonic fatigue. Int. J. Fatigue 27 (10–12), 1227–1232. http://dx.doi.org/10.1016/j.ijfatigue.2005.07.022.

Cheng, L., Gao, J., Kafka, O.L., Saha, S., Mojumder, S., Liu, W.K., 2020. Machine learning based methods for materials science and engineering. In: Proceedings of the 11th International Workshop on Meshfree Methods. Submitted for publication.

Cruzado, A., L. Lorca, J., Segurado, J., 2017. Modeling cyclic deformation of Inconel 718 superalloy by means of crystal plasticity and computational homogenization. Int. J. Solids Struct. 122–123, 148–161. http://dx.doi.org/10.1016/j.ijsolstr.2017.06.014.

Dehoff, R.R., Kirka, M., Sames, W.J., Bilheux, H., Tremsin, A.S., Lowe, L.E., Babu, S.S., 2015. Site specific control of crystallographic grain orientation through electron beam additive manufacturing. Mater. Sci. Technol. 31 (8), 931–938. http://dx.doi.org/10.1179/1743284714Y.0000000734.

Eghtesad, A., Zecevic, M., Lebensohn, R.A., McCabe, R.J., Knezevic, M., 2018. Spectral database constitutive representation within a spectral micromechanical solver for computationally efficient polycrystal plasticity modelling. Comput. Mech. 61 (1–2), 89–104. http://dx.doi.org/10.1007/s00466-017-1413-4.

Farahani, H.K., Ketabchi, M., Zangeneh, S., 2017. Determination of Johnson–Cook plasticity model parameters for Inconel 718. J. Mater. Eng. Perform. 26 (11), 5284–5293. http://dx.doi.org/10.1007/s11665-017-2990-2.

Ghorbanpour, S., Zecevic, M., Kumar, A., Jahedi, M., Bicknell, J., Jorgensen, L., Beyerlein, I.J., Knezevic, M., 2017. A crystal plasticity model incorporating the effects of precipitates in superalloys: Application to tensile, compressive, and cyclic deformation of Inconel 718. Int. J. Plast. 99, 162–185. http://dx.doi.org/10.1016/j.ijplas.2017.09.006.

Gockel, J., Sheridan, L., Koerper, B., Whip, B., 2019. The influence of additive manufacturing processing parameters on surface roughness and fatigue life. Int. J. Fatigue 124, 380–388. http://dx.doi.org/10.1016/j.ijfatigue.2019.03.025.

Gong, H., Rafi, K., Gu, H.F., Janaki Ram, G.D., Starr, T., Stucker, B., 2015. Influence of defects on mechanical properties of Ti-6Al-4V components produced by selective laser melting and electron beam melting. Mater. Des. 86, 545–554. http://dx.doi.org/10.1016/j.matdes.2015.07.147.

Gordon, J., Vinci, R., Hochhalter, J., Rollett, A., Harlow, D.G., 2019. Quantification of location-dependence in a large-scale additively manufactured build through experiments and micromechanical modeling. Materialia 7, 100397. http://dx.doi.org/10.1016/j.mtla.2019.100397.

Gorelik, M., 2017. Additive manufacturing in the context of structural integrity. Int. J. Fatigue 94, 168–177. http://dx.doi.org/10.1016/j.ijfatigue.2016.07.005.

Gribbin, S., Bicknell, J., Jorgensen, L., Tsukrov, I., Knezevic, M., 2016. Low cycle fatigue behavior of direct metal laser sintered Inconel alloy 718. Int. J. Fatigue 93, 156–167. http://dx.doi.org/10.1016/j.ijfatigue.2016.08.019.

Gürsoy, D.D., De Carlo, F., Xiao, X., Jacobsen, C., 2014. TomoPy: A framework for the analysis of synchrotron tomographic data. J. Synchrotron Radiat. 21 (5), 1188–1193. http://dx.doi.org/10.1107/S1600577514013939.

Heigel, J.C., Michaleris, P., Reutzel, E.W., 2015. Thermo-mechanical model development and validation of directed energy deposition additive manufacturing of Ti–6Al–4V. Addit. Manuf. 5, 9–19. http://dx.doi.org/10.1016/j.addma.2014.10.003.

Herroitt, C., Li, X., Kouraytem, N., Tari, V., Tan, W., Anglin, B., Rollett, A.D., Spear, A.D., 2019. A multi-scale, multi-physics modeling framework to predict spatial variation of properties in additive-manufactured metals. Modelling Simul. Mater. Sci. Eng. 27 (2), 025009. http://dx.doi.org/10.1088/1361-651x/aaf753.

Hohnbaum, C.C., 2019. Fracture Toughness and Fatigue Crack Growth Rate Characterization of IN718 Formed By Laser Powder Bed Fusion Air Force Institute of Technology (Ph.D. thesis). Air Force Institute of Technology.

Horstemeyer, M.F., 2010. Multiscale modeling: A review. In: Leszczynski, J., Shukla, M.K. (Eds.), Practical Aspects of Computational Chemistry: Methods, Concepts and Applications. Springer Netherlands, pp. 87–135.

Jinoop, A.N., Paul, C.P., Mishra, S.K., Bindra, K.S., 2019. Laser additive manufacturing using directed energy deposition of Inconel-718 wall structures with tailored characteristics. Vacuum 166, 270–278. http://dx.doi.org/10.1016/j.vacuum.2019.05.027.

Johnson, K.L., Emery, J.M., Hammetter, C.I., Brown, J.A., Grange, S.J., Ford, K.R., Bishop, J.E., 2019. Predicting the reliability of an additively-manufactured metal part for the third Sandia fracture challenge by accounting for random material defects. Int. J. Fract. 218 (1), 231–243. http://dx.doi.org/10.1007/s10704-019-00368-8.

Johnson, A.S., Shao, S., Shamsaei, N., Thompson, S.M., Bian, L., 2017. Microstructure, fatigue behavior, and failure mechanisms of direct laser-deposited Inconel 718. JOM 69 (3), 597–603. http://dx.doi.org/10.1007/s11837-016-2225-2.

Kafka, O.L., 2019. Experiment-Based Simulations for Heterogeneous Hierarchical Materials: Application to Metal Additive Manufacturing (Ph.D. thesis). Northwestern University.

Kafka, O.L., Yu, C., Shakoor, M., Liu, Z., Wagner, G.J., Liu, W.K., 2018. Data-driven mechanistic modeling of influence of microstructure on high-cycle fatigue life of nickel titanium. JOM 70 (7), 1154–1158. http://dx.doi.org/10.1007/s11837-018-2868-2.

Kasperovich, G., Hausmann, J., 2015. Improvement of fatigue resistance and ductility of TiAl6V4 processed by selective laser melting. J. Mater. Process. Technol. 220, 202–214. http://dx.doi.org/10.1016/j.jmatprotec.2015.01.025.

Kirka, M.M., Greeley, D.A., Hawkins, C., Dehoff, R.R., 2017. Effect of anisotropy and texture on the low cycle fatigue behavior of Inconel 718 processed via electron beam melting. Int. J. Fatigue 105, 235–243. http://dx.doi.org/10.1016/j.ijfatigue.2017.08.021.

Kumara, C., Deng, D., Moverare, J., Nylén, P., 2018. Modelling of anisotropic elastic properties in alloy 718 built by electron beam melting. Mater. Sci. Technol. 34 (5), 529–537. http://dx.doi.org/10.1080/02670836.2018.1426258.

Lass, E.A., Stoudt, M.R., Williams, M.E., Katz, M.B., Levine, L.E., Phan, T.Q., Gnaeupel-Herold, T.H., Ng, D.S., 2017. Formation of the Ni 3 Nb δ-phase in stress-relieved Inconel 625 produced via laser powder-bed fusion additive manufacturing. Metall. Mater. Trans. A 48 (11), 5547–5558. http://dx.doi.org/10.1007/s11661-017-4304-6.

Li, H., Kafka, O.L., Gao, J., Yu, C., Nie, Y., Zhang, L., Tajdari, M., Tang, S.Q.S., Guo, X., Li, G., Cheng, G.d., Liu, W.K., 2019a. Clustering discretization methods for generation of material performance databases in machine learning and design optimization. Comput. Mech. 64 (2), 281–305. http://dx.doi.org/10.1007/s00466-019-01716-0.

Li, X., Liu, Z., Cui, S.Q., Luo, C.C., Li, C.F., Zhuang, Z., 2019b. Predicting the effective mechanical property of heterogeneous materials by image based modeling and deep learning. Comput. Methods Appl. Mech. Engrg. 347, 735–753. http://dx.doi.org/10.1016/J.CMA.2019.01.005.

Li, P., Warner, D.H., Pegues, J.W., Roach, M.D., Shamsaei, N., Phan, N., 2019c. Towards predicting differences in fatigue performance of laser powder bed fused Ti-6Al-4V coupons from the same build. Int. J. Fatigue 126, 284–296. http://dx.doi.org/10.1016/j.ijfatigue.2019.05.004.

Liu, Z., Bessa, M.A., Liu, W.K., 2016. Self-consistent clustering analysis: An efficient multi-scale scheme for inelastic heterogeneous materials. Comput. Methods Appl. Mech. Engrg. 306, 319–341. http://dx.doi.org/10.1016/j.cma.2016.04.004.

Liu, Z., Kafka, O.L., Yu, C., Liu, W.K., 2018. Data-driven self-consistent clustering analysis of heterogeneous materials with crystal plasticity. In: Oñate, E., Peric, D., de Souza Neto, E., Chiumenti, M. (Eds.), Advances in Computational Plasticity: A Book in Honour of D. Roger J. Owen, Vol. 46. Springer International Publishing, pp. 221–242. http://dx.doi.org/10.1007/978-3-319-60885-3_11.

Liu, F., Lin, X., Huang, C., Song, M., Yang, G., Chen, J., Huang, W., 2011. The effect of laser scanning path on microstructures and mechanical properties of laser solid formed nickel-base superalloy Inconel 718. J. Alloys Compd. 509 (13), 4505–4509. http://dx.doi.org/10.1016/j.jallcom.2010.11.176.

Liu, P.W., Wang, Z., Xiao, Y.H., Lebensohn, R.A., Liu, Y.C., Horstemeyer, M.F., Cui, X.Y., Chen, L., 2019. Integration of phase-field model and crystal plasticity for the prediction of process-structure-property relation of additively manufactured metallic materials. Int. J. Plast. 128, 102670. http://dx.doi.org/10.1016/j.ijplas.2020.102670.

Ma, X.-F., Duan, Z., Shi, H.-J., Murai, R., Yanagisawa, E., 2010. Fatigue and fracture behavior of nickel-based superalloy Inconel 718 up to the very high cycle regime. J. Zhejiang Univ. Sci. A 11 (10), 727–737. http://dx.doi.org/10.1631/jzus.A1000171.

MacQueen, J., et al., 1967. Some methods for classification and analysis of multivariate observations. In: Proc. Fifth Berkeley Symp. on Math. Stat. and Probab., no. 14. Oakland, CA, USA. pp, 281–297.

Mills, K.C., 2002. Recommended Values of Thermophysical Properties for Selected Commercial Alloys. Woodhead Publishing.

Moussaoui, K., Rubio, W., Mousseigne, M., Sultan, T., Rezai, F., 2018. Effects of selective laser melting additive manufacturing parameters of Inconel 718 on porosity, microstructure and mechanical properties. Mater. Sci. Eng. A 735, 182–190. http://dx.doi.org/10.1016/j.msea.2018.08.037.

Mukherjee, T., DebRoy, T., 2018. Mitigation of lack of fusion defects in powder bed fusion additive manufacturing. J. Manuf. Process. 36, 442–449. http://dx.doi.org/10.1016/j.jmapro.2018.10.028.

Parimi, L.L., Ravi, G., Clark, D., Attallah, M.M., 2014. Microstructural and texture development in direct laser fabricated IN718. Mater. Charact. 89, 102–111. http://dx.doi.org/10.1016/j.matchar.2013.12.012.

Pei, C., Zeng, W., Yuan, H., 2020. A damage evolution model based on micro-structural characteristics for an additive manufactured superalloy under monotonic and cyclic loading conditions. Int. J. Fatigue 131, 105279. http://dx.doi.org/10.1016/j.ijfatigue.2019.105279.

Poulin, J.-R., Kreitcberg, A., Terriault, P., Brailovski, V., 2020. Fatigue strength prediction of laser powder bed fusion processed Inconel 625 specimens with intentionally-seeded porosity: Feasibility study. Int. J. Fatigue 132, 105394. http://dx.doi.org/10.1016/j.ijfatigue.2019.105394.

Prithivirajan, V., Sangid, M.D., 2018. The role of defects and critical pore size analysis in the fatigue response of additively manufactured IN718 via crystal plasticity. Mater. Des. 150, 139–153. http://dx.doi.org/10.1016/j.matdes.2018.04.022.

Ressa, A., 2015. Plastic Deformation and Ductile Fracture Behavior of Inconel 718 (Masters). The Ohio State University, http://dx.doi.org/10.1145/3132847.3132886.

Rodgers, T.M., Bishop, J.E., Madison, J.D., 2018. Direct numerical simulation of mechanical response in synthetic additively manufactured microstructures. Modelling Simul. Mater. Sci. Eng. 26 (5), http://dx.doi.org/10.1088/1361-651X/aac616.

Sanaei, N., Fatemi, A., Phan, N., 2019. Defect characteristics and analysis of their variability in metal L-PBF additive manufacturing. Mater. Des. 182, 108091. http://dx.doi.org/10.1016/J.MATDES.2019.108091.

Seifi, M., Gorelik, M., Waller, J., Hrabe, N., Shamsaei, N., Daniewicz, S., Lewandowski, J.J., 2017a. Progress towards metal additive manufacturing standardization to support qualification and certification. JOM 69 (3), 439–455. http://dx.doi.org/10.1007/s11837-017-2265-2.

Seifi, M., Salem, A., Satko, D., Shaffer, J., Lewandowski, J.J., 2017b. Defect distribution and microstructure heterogeneity effects on fracture resistance and fatigue behavior of EBM Ti–6Al–4V. Int. J. Fatigue 94, 263–287. http://dx.doi.org/10.1016/j.ijfatigue.2016.06.001.

Shakoor, M., Kafka, O.L., Yu, C., Liu, W.K., 2018. Data science for finite strain mechanical science of ductile materials. Comput. Mech. 64 (1), 33–45. http://dx.doi.org/10.1007/s00466-018-1655-9.

Shamsaei, N., Yadollahi, A., Bian, L., Thompson, S.M., 2015. An overview of direct laser deposition for additive manufacturing; Part II: Mechanical behavior, process parameter optimization and control. Addit. Manuf. 8, 12–35. http://dx.doi.org/10.1016/j.addma.2015.07.002.

Shenoy, M., Zhang, J., McDowell, D.L., 2007. Estimating fatigue sensitivity to polycrystalline Ni-base superalloy microstructures using a computational approach. Fatigue Fract. Eng. Mater. Struct. 30 (10), 889–904.

Sheridan, L., Scott-Emuakpor, O.E., George, T., Gockel, J.E., 2018. Relating porosity to fatigue failure in additively manufactured alloy 718. Mater. Sci. Eng. A 727, 170–176. http://dx.doi.org/10.1016/j.msea.2018.04.075.

Smith, J., Xiong, W., Cao, J., Liu, W.K., 2016. Thermodynamically consistent microstructure prediction of additively manufactured materials. Comput. Mech. 57 (3), 359–370. http://dx.doi.org/10.1007/s00466-015-1243-1.

Tabernero, I., Lamikiz, A., Martınez, S., Ukar, E., Figueras, J., 2011. Evaluation of the mechanical properties of Inconel 718 components built by laser cladding. Int. J. Mach. Tools Manuf. 51 (6), 465–470. http://dx.doi.org/10.1016/j.ijmachtools.2011.02.003.

Tallman, A.E., Swiler, L.P., Wang, Y., McDowell, D.L., 2020. Uncertainty propagation in reduced order models based on crystal plasticity. Comput. Methods Appl. Mech. Engrg. 365, 113009. http://dx.doi.org/10.1016/j.cma.2020.113009.

Texier, D., Cormier, J., Villechaise, P., Stinville, J.-C.C., Torbet, C.J., Pierret, S., Pollock, T.M., 2016. Crack initiation sensitivity of wrought direct aged alloy 718 in the very high cycle fatigue regime: The role of non-metallic inclusions. Mater. Sci. Eng. A 678, 122–136. http://dx.doi.org/10.1016/j.msea.2016.09.098.

Whelan, G., McDowell, D.L., 2019. Uncertainty quantification in ICME workflows for fatigue critical computational modeling. Eng. Fract. Mech. 220, http://dx.doi.org/10.1016/j.engfracmech.2019.106673.

Witkin, D.B., Patel, D.N., Bean, G.E., 2019. Notched fatigue testing of Inconel 718 prepared by selective laser melting. Fatigue Fract. Eng. Mater. Struct. 42 (1), 166–177. http://dx.doi.org/10.1111/ffe.12880.

Wolff, S.J., Lin, S.E., Faierson, E.J., Liu, W.K., Wagner, G.J., Cao, J., 2017. A framework to link localized cooling and properties of directed energy deposition (DED)-processed Ti-6Al-4V. Acta Mater. 132, 106–117. http://dx.doi.org/10.1016/j.actamat.2017.04.027.

Yadollahi, A., Shamsaei, N., 2017. Additive manufacturing of fatigue resistant materials: Challenges and opportunities. Int. J. Fatigue 98, 14–31. http://dx.doi.org/10.1016/j.ijfatigue.2017.01.001.

Yan, N., Kawagoishi, N., Chen, Q., Wang, Q.Y., Nisitani, H., Kondo, E., 2003. Fatigue properties of Inconel 718 in long life region at elevated temperature. Key Eng. Mater. 243–244, 321–326. http://dx.doi.org/10.4028/www.scientific.net/KEM.243-244.321.

Yan, W., Lian, Y.P., Yu, C., Kafka, O.L., Liu, Z., Liu, W.K., Wagner, G.J., 2018a. An integrated process—structure—property modeling framework for additive manufacturing. Comput. Methods Appl. Mech. Engrg. 339, 184–204. http://dx.doi.org/10.1016/j.cma.2018.05.004.

Yan, F., Xiong, W., Faierson, E., Olson, G.B., 2018b. Characterization of nano-scale oxides in austenitic stainless steel processed by powder bed fusion. Scr. Mater. 155, 104–108. http://dx.doi.org/10.1016/j.scriptamat.2018.06.011.

Yu, C., 2019. Multiscale Clustering Analysis (Ph.D. thesis). Northwestern University.

Yu, C., Kafka, O.L., Liu, W.K., 2019. Self-consistent clustering analysis for multiscale modeling at finite strains. Comput. Methods Appl. Mech. Engrg. 349, 339–359. http://dx.doi.org/10.1016/j.cma.2019.02.027.

Yuan, K., Guo, W., Li, P., Wang, J., Su, Y., Lin, X., Li, Y., 2018. Influence of process parameters and heat treatments on the microstructures and dynamic mechanical behaviors of Inconel 718 superalloy manufactured by laser metal deposition. Mater. Sci. Eng. A 721, 215–225. http://dx.doi.org/10.1016/j.msea.2018.02.014.

Zhang, Y.Y., Duan, Z., Shi, H., 2013. Comparison of the very high cycle fatigue behaviors of Inconel 718 with different loading frequencies. Sci. China Phys. Mech. Astron. 56 (3), 617–623. http://dx.doi.org/10.1007/s11433-013-5013-9.

Zhao, X., Chen, J., Lin, X., Huang, W., 2008. Study on microstructure and mechanical properties of laser rapid forming Inconel 718. Mater. Sci. Eng. A 478 (1), 119–124. http://dx.doi.org/10.1016/j.msea.2007.05.079.